

Laser Damage Threshold of Hydrophobic Up-Conversion Carboxylated Nanocellulose/SrF₂:Ho Composite Films Functionalized With 3-Aminopropyltriethoxysilane

Anna A. Luginina

Prokhorov General Physics Institute RAS: Institut obsej fiziki imeni A M Prohorova RAN

Sergey V. Kuznetsov

Prokhorov General Physics Institute RAS: Institut obsej fiziki imeni A M Prohorova RAN

Vladimir K. Ivanov

Kurnakov Institute of General and Inorganic Chemistry RAS: Institut obsej i neorganiceskoj himii imeni N S Kurnakova RAN

Valery V. Voronov

Prokhorov General Physics Institute RAS: Institut obsej fiziki imeni A M Prohorova RAN

Alexey D. Yaprntsev

Kurnakov Institute of General and Inorganic Chemistry RAS: Institut obsej i neorganiceskoj himii imeni N S Kurnakova RAN

Andrey A. Lyapin

Ogarev Mordovia State University: Nacional'nyj issledovatel'skij Mordovskij gosudarstvennyj universitet imeni N P Ogareva

Elena V. Chernova

Prokhorov General Physics Institute RAS: Institut obsej fiziki imeni A M Prohorova RAN

Aleksandr A. Pynenkov

Ogarev Mordovia State University: Nacional'nyj issledovatel'skij Mordovskij gosudarstvennyj universitet imeni N P Ogareva

Konstantin N. Nishchev

Ogarev Mordovia State University: Nacional'nyj issledovatel'skij Mordovskij gosudarstvennyj universitet imeni N P Ogareva

Radmir V. Gainutdinov

Shubnikov Institute of Crystallography RAS: FGU Federal'nyj naucno-issledovatel'skij centr Kristallografia i fotonika Rossijskoj akademii nauk

Alexey V. Bogach

Prokhorov General Physics Institute RAS: Institut obsej fiziki imeni A M Prohorova RAN

Pavel P. Fedorov (✉ ppfedorov@yandex.ru)

Prokhorov General Physics Institute RAS: Institut obsej fiziki imeni A M Prohorova RAN

<https://orcid.org/0000-0002-2918-3926>

Research Article

Keywords: TEMPO-oxidized cellulose nanofibrils, Functionalization, Nanocomposite, SrF₂:Ho, Up-50 conversion luminescence

Posted Date: May 11th, 2021

DOI: <https://doi.org/10.21203/rs.3.rs-461271/v1>

License: © ⓘ This work is licensed under a Creative Commons Attribution 4.0 International License.

[Read Full License](#)

1 **Laser damage threshold of hydrophobic up-conversion carboxylated**
2 **nanocellulose/SrF₂:Ho composite films functionalized with 3-aminopropyltriethoxysilane**

3
4 Anna A. Luginina^a, Sergey V. Kuznetsov^a, Vladimir K. Ivanov^b, Valery V. Voronov^a, Alexey D.
5 Yapryntsev^b, Andrey A. Lyapin^c, Elena V. Chernova^a, Aleksandr A. Pynenkov^c, Konstantin N.
6 Nishchev^c, Radmir V. Gainutdinov^d, Alexey V. Bogach^a, Pavel P. Fedorov^a

7
8 ^aProkhorov General Physics Institute, Russian Academy of Sciences, 38 Vavilov Street, Moscow
9 119991, Russia

10 ^bKurnakov Institute of General and Inorganic Chemistry, Russian Academy of Sciences, 31
11 Leninsky Prospect, Moscow 119991, Russia

12 ^cOgarev Mordovia State University, 68 Bolshevistskaya str., Saransk, 430005, Russia

13 ^dShubnikov Institute of Crystallography, Federal Scientific Research Centre Crystallography and
14 Photonics, Russian Academy of Sciences, 59 Leninsky Prospect, Moscow, 119333, Russia

15
16 **Corresponding author:** P.P. Fedorov, ORCID <https://orcid.org/0000-0002-2918-3926>, E-mail:
17 ppfedorov@yandex.ru; Tel: +7(499)503-87-92

18
19
20 **Acknowledgments**

21 This work was supported by the Ministry of Science and Higher Education within the State
22 assignment to Prokhorov General Physics Institute of the Russian Academy of Sciences and
23 FSRC Crystallography and Photonics RAS. The equipment of the Shared Research Center
24 supported by the Ministry of Science and Higher Education (RFMEFI62114X0005) was used in
25 experiments. Authors express their sincere gratitude to Dr. Arthur I. Popov for his most kind
26 assistance in the preparation of the present manuscript and Dr. Vladimir N. Kuryakov for zeta
27 potential measurements.

29 **Abstract**

30 Luminescent nanocomposite films, containing SrF₂:Ho up-conversion particles, were prepared
31 by two different protocols from aqueous dispersions of TEMPO-oxidized cellulose nanofibrils
32 (TOCNF) functionalized with 3-aminopropyltriethoxysilane (APS) without the use of organic
33 solvents at pH = 4.0-4.5 and 9.0-9.5, respectively. Proposed synthetic protocols included
34 formation of the films by drying the dispersions containing pre-hydrolyzed APS adsorbed onto
35 TOCNF and SrF₂:Ho particles followed by heating at 105 °C. Hydrophobic (water contact angle
36 $101 \pm 2^\circ$), strong, and translucent TOCNF/SrF₂:Ho-APS films were prepared by casting from a
37 solution at pH = 4.0-4.5. Scanning electron microscopy, energy-dispersive X-ray spectroscopy
38 with element mapping, Fourier-transform infrared spectroscopy, X-ray diffraction methods
39 confirmed homogeneous distribution of up-conversion particles in TOCNF matrices as well as
40 the grafting of linear polysiloxanes via the condensation of silanol groups and OH-groups on the
41 surface of TOCNF. Differential scanning calorimetry and thermogravimetry data confirmed an
42 increase in thermal stability of the APS modified nanocomposite films obtained at pH = 4.0-4.5.
43 Hydrophobic TOCNF/SrF₂:Ho-APS nanocomposite films exhibited an intense red luminescence
44 in the visible spectrum range (⁵I₇ level excitation of Ho³⁺ ions with 1912 nm laser irradiation)
45 as well as two-times higher laser damage threshold compared to unmodified TOCNF/SrF₂:Ho
46 films. TOCNF/SrF₂:Ho films can be used for visualization 2 μm laser radiation in medicine and
47 long-distance atmosphere monitoring.

48

49 **Keywords**

50 TEMPO-oxidized cellulose nanofibrils; Functionalization; Nanocomposite; SrF₂:Ho; Up-
51 conversion luminescence

52

53

54 Introduction

55

56 New generation luminescent nanocellulose-based composites and hybrid materials have found
57 numerous application in optoelectronics (Dias et al. 2020; Vicente et al. 2018; Yang et al. 2018),
58 organic light-emitting diodes (OLEDs) (Zhang et al. 2019), biosensors and detectors for
59 monitoring environment and/or food quality control (Dai et al. 2020; Wang et al. 2020),
60 biomedicine (Guan et al. 2018), latent finger print detection (Hai et al. 2018), anti-counterfeiting
61 applications (Li and Hu 2019; Xiong et al. 2019; Zhang et al. 2018) and some other areas of
62 photonics (Eichhorn 2018; Lizundia et al. 2020; Xue et al. 2018; Zhang et al. 2017). Cellulose
63 nanofibrils (CNF), cellulose nanocrystals (CNC) and TEMPO-oxidized CNF (TOCNF) are
64 unique matrices for the synthesis of luminescent nanocomposites because of their large surface
65 areas, high reactivities, good optical properties, mechanical strength and colloid stability (De
66 France et al. 2020; Kontturi et al. 2018; Thomas et al. 2018). Rare earth-based up-conversion
67 luminophores, that efficiently transform near-infrared irradiation to visible light (Auzel 2004;
68 Dong et al. 2013; Ovsyankin and Feofilov 1966; Qin et al. 2017; Reig et al. 2020), can be
69 utilized for object visualization, biomarkers, luminescent tagging, solar elements, electronic
70 displays, etc. (Brites et al. 2020; Fischer et al. 2018; Liang et al. 2019; Zhou et al. 2015); this
71 includes two-micron laser irradiation visualizers, based on holmium luminescent transitions,
72 implemented in medical equipment and lidars (Belyaev et al. 2016; Lyapin et al. 2017; Scholle et
73 al. 2010; Verber et al. 1971). Metal fluorides are considered most effective luminophore
74 matrices because of low phonon energies and high probabilities of the anti-Stokes transitions
75 allowing visualization of IR- irradiation (Fedorov et al. 2011).

76 Composites based on nanocellulose and up-conversion luminophores have allowed developing
77 the novel optical devices because of the synergy between the components. For example, the
78 combination of CNC and 2.8 wt. % NaYF₄:Yb:Er cubic phase was used for chiral up-conversion
79 luminescent films preparation by evaporation-induced self-assembly (EISA) technique (Jiang et
80 al. 2016). Up-conversion luminescent films, retaining tunable photonic chiral activity, have been
81 obtained by self-assembly of CNC and polyvinyl alcohol (PVA)-stabilized hexagonal
82 NaYF₄:Yb,Er nanorods (Nguyen et al. 2017). Up-conversion luminescent nanopaper, comprising
83 cellulose nanofibrils (CNF) functionalized with NaYF₄:Yb,Er nanoparticles, have been
84 synthesized for prospective applications in sensors and anticounterfeiting labels (Zhao et al.
85 2014).

86 Laser damage threshold (Wood 2014) and thermal stability (Delone 1993) are important criteria
87 of nanocomposite film stability and their applicability as IR-irradiation visualizers. Earlier, we
88 have developed flexible semitransparent CNC and CNC/CNF composite films with up-
89 conversion SrF₂:Ho particles (Fedorov et al. 2019) and hydrophobic TOCNF-based alkyl ketene
90 dimer (AKD) modified composite films with up-conversion MF₂:Ho (M = Ca, Sr) particles
91 (Fedorov et al. 2020). These composites demonstrated intense red luminescence under Ho³⁺
92 excitation with 1912 nm laser irradiation.

93 Considering that nanocomposite films have to be flexible and thermally stable, we have chosen
94 TOCNF as the matrix for the incorporation of SrF₂:Ho nanoparticles. Significant amount of OH⁻
95 and COO⁻ groups on TOCNF surface opens opportunity for the surface modification, including
96 increasing TOCNF thermal stability and hydrophobization of TOCNF surface (Rol et al. 2019),
97 for example, by silylation. CNF silylation is carried out with various silylating agents, including
98 methyltrichlorosilane (Orsolini et al. 2018), hexamethyldisilazone (Johansson et al. 2011),
99 trimethylchlorosilane (Sai et al. 2015), chlorodimethylisopropylsilane (Andresen et al. 2006), 3-
100 aminopropyltriethoxysilane (APS) (Peresin et al. 2017) in organic solvents. Salon et al. (2007)
101 studied modification of microcrystalline cellulose with APS in ethanol/water and established that
102 APS hydrolysis with the formation of silanol groups was required in order to enhance cellulose
103 grafting, but covalent bonding of silanol groups with cellulose hydroxyls occurred only after the
104 thermal treatment at 100-110°C. Also, Robles et al. (2018) studied CNF silylation with APS in
105 ethanol, water, and ethanol/water media and observed formation of hydrophobic CNF-APS films

106 when water was used as a reaction solvent. Khanjanzadeh et al. (2018) performed CNC silylation
107 with APS in aqueous solutions: at the beginning, APS was hydrolyzed in water, adsorbed onto
108 CNC with hydrogen bond formation, covalently bound to CNC by forming Si-O-C bonds with
109 CNC surface after reaction between silanol groups and CNC hydroxyls, resulting in an increase
110 of thermal stability (by $\sim 10^{\circ}\text{C}$) of silylated CNC compared to untreated material. Interestingly,
111 we have found only a single report of TOCNF silylation with APS in ethanol/water solutions
112 (Indarti et al. 2019). Whereas silylation of CNC and CNF is an efficient way of their
113 hydrophobization, and some authors (Khanjanzadeh et al. 2018; Sai et al. 2015) mentioned
114 increase of thermal stability of organosilylated CNC and CNF, similar effects for TOCNF have
115 not been reported yet.

116 In this paper, we chose readily available and inexpensive bifunctional APS monomer with
117 primary amino-group and easily hydrolyzable ethoxysilyl moiety as silylating agent because of
118 its high reaction capability, good solubility in water and low toxicity.

119 The purpose of the present study was to develop of up-converting nanocomposite
120 TOCNF/SrF₂:Ho-APS films with hydrophobic properties and enhanced thermal stability as well
121 as increased laser damage threshold compared to earlier reported composite films (Fedorov et al.
122 2019, 2020). TOCNF/SrF₂:Ho-APS nanocomposite films were obtained by mixing aqueous
123 TOCNF dispersion, up-conversion SrF₂:Ho particles and aqueous APS in different weight ratios
124 followed by casting, drying under air and thermal treatment. The hydrophobicity, morphological,
125 structural, and thermal properties of the composite films were studied depending on the pH of
126 the reaction medium, the content of up-conversion particles and APS. We also studied optical
127 and luminescent properties of obtained composite films as well as their laser damage threshold.

128

129 **Materials and methods**

130

131 Starting Materials

132

133 Ash free filter paper (FP) “Blue Ribbon” (I β crystal structure, crystallinity index 68.7, degree of
134 polymerization 1112, particle width 25-30, particle length 200-1500 μm , Table S1); TEMPO
135 (99% pure; manufactured by NIOCH SB RAS, Russia); 3-aminopropyltriethoxysilane (97%
136 pure; manufactured by PENTA-91 company, Russia); 19 wt.% sodium hypochlorite solution;
137 sodium bromide; sodium hydroxide; acetic acid and hydrochloric acid (99.9% pure); double
138 distilled water (regenerated cellulose dialysis tube, 12–14 kDa molecular weight cut-off,
139 manufactured by Orange Scientific, Belgium); and up-conversion Sr_{1-x}Ho_xF_{2+x} (x = 0.08 and
140 0.10) powders were used as starting materials. Sr_{1-x}Ho_xF_{2+x} fluoride luminophores were prepared
141 by the technique proposed earlier (Fedorov et al., 2017).

142

143 TOCNF preparation

144

145 TOCNF was prepared by the previously reported technique (Jiang et al. 2013) with some
146 modifications. 10.00 g of ground FP were soaked in 312 ml double distilled water, obtained
147 mixture was diluted with 312 ml 11.7 M HCl, placed in 80°C water bath, hydrolyzed at the same
148 temperature under constant stirring for 20 min, and quenched with 10-fold excess of cold double
149 distilled water. Obtained suspension was further washed with double distilled water until pH
150 value reached about 5.0, and sonicated in an ice bath for 15 min. Cellulose content in the
151 obtained product was determined by gravimetric analysis. Obtained suspension of 10 g cellulose
152 in about 800 ml water was treated with 200 ml aqueous solution of 0.1600 g TEMPO and 1.0000
153 g NaBr, stirred for 10 min at room temperature, oxidized by slowly added 11.9 wt% NaClO (10
154 mmol/g cellulose) under constant stirring at room temperature. pH (10.0-10.5) was maintained
155 by adding 0.3 M NaOH. Oxidative treatment was stopped after pH stabilized, and reaction
156 mixture was mixed with 0.5 M HCl to achieve pH 7. Then, about 100 ml water was added to the
157 decanted precipitate, stirred up and centrifuged at 7,500 rpm for 10 min. Obtained precipitate

158 ultrasonicated in double distilled water in ice bath for 15 min, dialyzed against water flow for 7
159 days, and once again ultrasonicated in double distilled water in ice bath for 15 min. TOCNF
160 dispersion was stored at 4 °C. TOCNF content in the dispersion was determined by gravimetry.
161 TOCNF yield was about 70%.

162

163 Preparation of silylated TOCNF

164

165 We used APS/dry TOCNF 0.44, 0.66, 1.11, 1.22, 1.33, 1.44, 1.48 and 1.55 weight ratio that
166 corresponds to APS loading of 2.0, 3.0, 5.0, 5.5, 6.0, 6.5, 6.7 and 7.0 mmol/g dried TOCNF.
167 TOCNF modification was carried out in an aqueous medium at pH = 9.0-9.5 and pH = 4.0-4.5;
168 silylation was performed as reported elsewhere (Khanjanzadeh et al. 2018; Tan et al. 2016), see
169 protocols 1 and 2, respectively.

170

171 *Silylation in water at pH 9-9.5 (Protocol 1)*

172

173 This protocol was based on the report of Tan et al. (2016). APS aqueous solutions (1.19-4.16
174 wt.%) were prepared by adding APS to double distilled water under intense stirring in
175 fluoroplastic beaker for 10 min. Then, 10.0000 g of TOCNF dispersion (1.88 wt.%) were added
176 dropwise to APS solution and stirred with magnetic stirrer at room temperature for 30 min, while
177 maintaining pH value in 9.0-9.5 range by adding dropwise 0.1 wt% NaOH. APS concentration
178 increased from 0.49 to 1.71 wt%, while TOCNF concentration was constant (about 1.10 wt%).
179 The films were formed by pouring the obtained mixture in polystyrene Petri dishes, drying at
180 room temperature for 2 days and at 105°C for 60 min (Khanjanzadeh et al 2018). Obtained films
181 (45-55 micron thickness) were cooled in P₂O₅-dried desiccator in order to prevent the formation
182 of bicarbonated amino groups through the reaction with water and atmospheric carbon dioxide.
183 The films were designated TOCNF-bAPS_n, where b is means pH= 9.0-9.5 of the reaction
184 medium, and n is APS loading equal to the ratio of APS to dried TOCNF, mmol/g.

185

186 *Silylation in water at pH 4-4.5 (Protocol 2)*

187

188 This protocol was based on the report of Khanjanzadeh et al. (2018) with the same precursor
189 content/concentration as in Protocol 1; while the synthesis was carried out at pH= 4.0-4.5. pH
190 value was corrected with ice acetic acid, and obtained modified films were labeled as TOCNF-
191 APS_n.

192

193 Preparation of modified nanocomposite films

194

195 In order to obtain nanocomposite films, Sr_{1-x}Ho_xF_{2+x} (x = 0.08 и 0.10) powder, annealed at
196 750°C, was thoroughly ground in an agate mortar. 0.1000-0.2900 g of ground powder were
197 dispersed in 10.0000 g TOCNF (1.88 wt.%) colloid suspension under ultrasonication in an ice
198 bath for 3-5 min until mixture cooling was completed (total treatment time was about 15 min).
199 Unmodified nanocomposite films with the same holmium content were prepared under the
200 similar conditions (see Supplementary Information Experimental method SM1). Obtained
201 dispersion was added dropwise to APS solution prepared by protocol 1 or 2 stirred with a
202 magnetic stirrer at room temperature for 30 min, while maintaining the pH value of 9.0-9.5 or
203 4.0-4.5, respectively. Composite films (50-60 micron thickness) were formed by pouring the
204 obtained mixture in polystyrene Petri dishes, drying at room temperature for 2 days and at 105°C
205 for 60 min and cooling in desiccator with P₂O₅. The dried films contained 30-56 wt.%
206 nanocellulose and 3.0-5.5 wt.% Ho. Films obtained at pH= 9.0-9.5 were labeled as TOCNF:xHo-
207 bAPS_n where x is holmium wt% content.

208

209 Characterization

210
211 X-ray diffraction patterns were recorded with Bruker D8 Advance diffractometer (Bruker AXS
212 GmbH, Karlsruhe, Germany; CuK α -radiation; 8–60° 2 θ range, 0.02° 2 θ step). The 22.7° 2 θ
213 diffraction peak was used for TOCNF crystallinity index (IC, %) calculation by Segal's method
214 (Fedorov et al 2019).

215 The carboxylate content (mmol/g) in TOCNF was determined by a conductometric titration
216 technique according to the protocol described elsewhere (Jiang et al. 2013). The conductivity
217 values were recorded at room temperature using an Expert-002 conductometer as the mean value
218 of three measurements. The degree of oxidation of primary hydroxyl groups (DO) was
219 determined by Equation 1 (Habibi et al. 2006):

$$220 \quad DO = \frac{162 \times (V_1 - V_0) \times C_{NaOH}}{m - 36 \times (V_1 - V_0) \times C_{NaOH}} \quad (1),$$

221 where V_1 and V_0 are the equivalent volumes of NaOH standard solution added (in L); C_{NaOH} is
222 the exact concentration of NaOH standard solution (mol/L); m is dry TOCNF weight in TOCNF
223 dispersion (g); and coefficients 162 and 36 correspond to the molecular weight of
224 anhydroglucose unit (AGU) and the difference between molecular weights of AGU and sodium
225 anhydroglucuronate moiety, respectively.

226 The particle distributions in the films were analyzed by simultaneous use of scanning electron
227 microscopy (SEM) and energy-dispersive X-ray spectroscopy (EDX) (NVision 40 microscope,
228 Carl Zeiss NTS GmbH, Germany, with X-Max detector, Oxford Instruments, UK). The surface
229 morphology, size, and shape of TOCNF particles and the morphology of composite films were
230 also analyzed using SEM. A drop of dilute aqueous dispersion of 0.01 wt.% TOCNF was applied
231 onto a single crystal silicon substrate and air-dried for the SEM further analysis. Particle size,
232 size of nanofibrils, and pore size were calculated using the ImageJ software as a mean value in
233 25 independent measurements.

234 The surface morphology and roughness were investigated using NTEGRA Prima atomic force
235 microscope (NTMDT Spectrum Instruments, Russia) in a tapping mode. All experiments were
236 carried out under controlled conditions maintained by a TRACKPORE ROOM-05 measuring
237 complex (purity class 5 ISO (100), the accuracy of maintaining air temperature in the range of 23
238 \pm 5 K is \pm 0.05 K, the relative air humidity is 55 \pm 1%). The average roughness (Ra) was
239 measured using the atomic force microscopy (AFM) images for 10 μ m \times 10 μ m scanning areas.

240 Zeta potential (ζ -potential) values of the dispersions were measured by electrophoretic light
241 scattering technique using the phase analysis light scattering (PALS) on the Photocor Compact-Z
242 analyzer at room temperature. The resulting ζ -potential values are mean values in five
243 consecutive measurements.

244 The degree of polymerization (DP) was assessed by viscosity measurements using diluted
245 solutions of dry nanocellulose films in Cadoxen (cadmium ethylenediamine) (Voronova et al.
246 2017). DP was determined as an average of two independent measurements.

247 The thickness of each film was determined by a micrometer (MKTS-25 0.001, Kalibron, Russia)
248 as the mean value for seven randomly selected locations.

249 Fourier transform infrared spectroscopy (FTIR) studies were performed on an INFRALUM FT-
250 08 spectrometer equipped with ATR unit (Pike) in the range from 400 to 4000 cm^{-1} .

251 The transmission spectra were recorded in the 250–3000 nm range using a Cary 5000
252 spectrophotometer.

253 Differential scanning calorimetry (DSC) and thermal gravimetric analysis (TGA) were
254 performed on a Netzsch DSC 404 F1 Pegasus and Netzsch TG 209 F1 Libra devices in the range
255 from 25 to 800°C with a 5°C/min heating rate under air.

256 The water contact angle was measured on a FTA1000 Drop Shape Instrument B Frame System.
257 The test sample was placed on a horizontal holder. The water was applied onto the surface of the
258 test sample by a special microdosing syringe. The droplet volume was 100 μ l. The images were
259 recorded using a 640x480 pixel CCD detector. Images were obtained in 1 s and 60 s after the

260 application of droplets. The measurements were performed at room temperature ($24 \pm 2^\circ\text{C}$) and
261 repeated for 5 times on various fresh surfaces.

262 In order to determine holmium content in the synthesized nanocomposite films, they were heated
263 at 730°C for 1 hour under air. Obtained annealed fluoride powder residue was converted to
264 sulphates by heating with concentrated sulfuric acid followed by evaporation of liquid phase
265 until dryness. Formed sulfates were dissolved in water and titrated with disodium
266 ethylenediaminetetraacetate (xylenol orange indicator) (see Supplementary Information
267 Experimental method SM2).

268 The up-conversion luminescence spectra were recorded with a Horiba FHR 1000
269 spectrophotometer. A continuous solid-state $\text{LiYF}_4:\text{Tm}$ laser, operating at 1912 nm, was used as
270 the excitation source for Ho^{3+} ions. The beam diameter and excitation power of incident laser
271 radiation were $300\ \mu\text{m}$ and 960 mW, respectively.

272 The damage threshold, being the characteristic of laser radiation durability, was detected visually
273 by observation of the film sample destruction under 1940 nm laser irradiation with focused laser
274 beam with $1500\ \mu\text{m}$ (1.5 mm) diameter. Fiber TLM-10 laser (IPF Photonics) was used as an
275 excitation source.

276

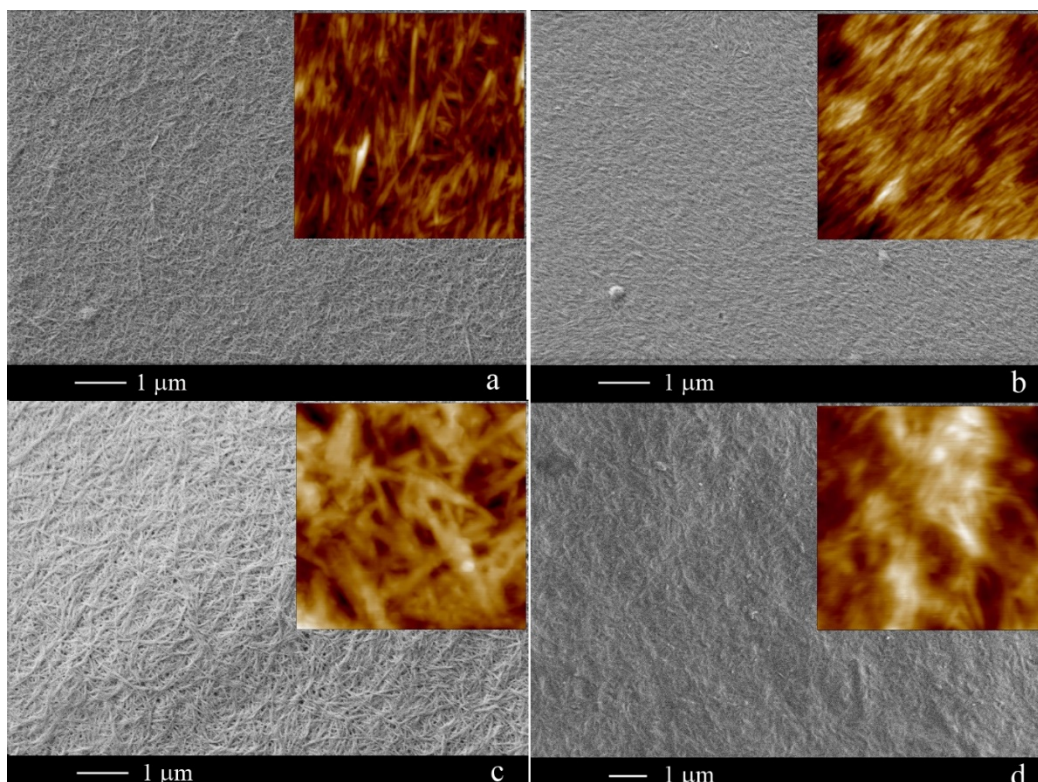
277 **Results and discussion**

278

279 Morphology of TOCNF, TOCNF-APS, TOCNF-bAPS films, suspension stability of TOCNF-
280 APS, TOCNF-bAPS, TOCNF:Ho-APS, TOCNF:Ho-bAPS and hydrophobic properties of the
281 films

282

283 Obtained transparent aqueous TOCNF dispersions (1.20 ± 0.05 mmol/g carboxyl group content;
284 oxidation degree $\text{DO} = 0.20$ that corresponded to one oxidized primary hydroxyl per five
285 anhydroglucose units) maintained their stability for at least 6 months (Figs. S1a, b); -50 ± 2 mV
286 ζ -potential. The colloidal stability was ensured by electrostatic repulsion of COO^- functional
287 groups: both TOCNF chemical structure and selective oxidation of primary hydroxyls at C6 are
288 well described in the literature (Okita et al. 2010). HCl hydrolysis followed by TEMPO
289 oxidation lowered TOCNF degree of polymerization down to 123 ± 3 (Table S1), i.e., by about an
290 order of magnitude. SEM images of TOCNF samples contain entangled nanofibrils (20 ± 6 nm
291 width, 809 ± 98 nm length) forming porous network (Fig. 1a) which is in a good agreement with
292 AFM data. CNC films obtained by previously reported protocol (Fedorov et al 2019), consist of
293 short needle-type rods with 14 ± 2 nm width and 107 ± 38 nm length aligned in the same
294 direction (Fig. 1b). CNC thickness is more uniform than TOCNF thickness (Table 1).



295
296

297 **Fig. 1** SEM images of 0.01 wt.% dispersions air-dried on a single-crystal silicon substrate:
298 TOCNF (a), CNC (b). SEM images of films after thermal treatment at 105 °C: TOCNF-APS_{7.00}
299 (c), TOCNF-bAPS_{7.0} (d). Insets show the corresponding film images obtained by AFM (1 μm ×
300 1 μm scanning area)

301

302 TOCNF silylation with APS in aqueous medium was carried out according to two protocols.
303 APS aqueous solutions maintained their stability at pH 9.0-9.5 and/or pH 4-4.5 for at least one
304 month (Figs. S1c, d). 0.10 wt.% TOCNF and 0.15 wt.% APS mixed dispersions were also stable
305 within the same time periods (-30 ± 3 mV and -17 ± 2 mV ζ -potentials for TOCNF-bAPS_{6.7} and
306 TOCNF-APS_{6.7}, dispersions, respectively; Fig. S1e, f). The decrease in the absolute value of ζ -
307 potential for TOCNF-APS_{6.7} in comparison with TOCNF-bAPS_{6.7} was probably caused by
308 amino-group protonation, leading to the increase in the ionic strength of the system and
309 contraction of the double electric layer.

310 1.10 wt.% TOCNF and 0.98 wt.% APS dispersions maintained their stability without
311 flocculation and/or sedimentation for at least 5 days (Figs. S1g, h). These dispersions were more
312 transparent and viscous at pH 9.0-9.5 than at pH 4-4.5, due to their three dimensional structure
313 (T^3 units) formed as a result of silanetriol self-condensation (Beari et al. 2001, Salon et al. 2007,
314 Salon et al. 2010).

315

316 **Table 1** Physical properties of TOCNF, CNC, TOCNF-APS_{7.0}, TOCNF-bAPS_{7.0} films after
317 thermal treatment at 105°C

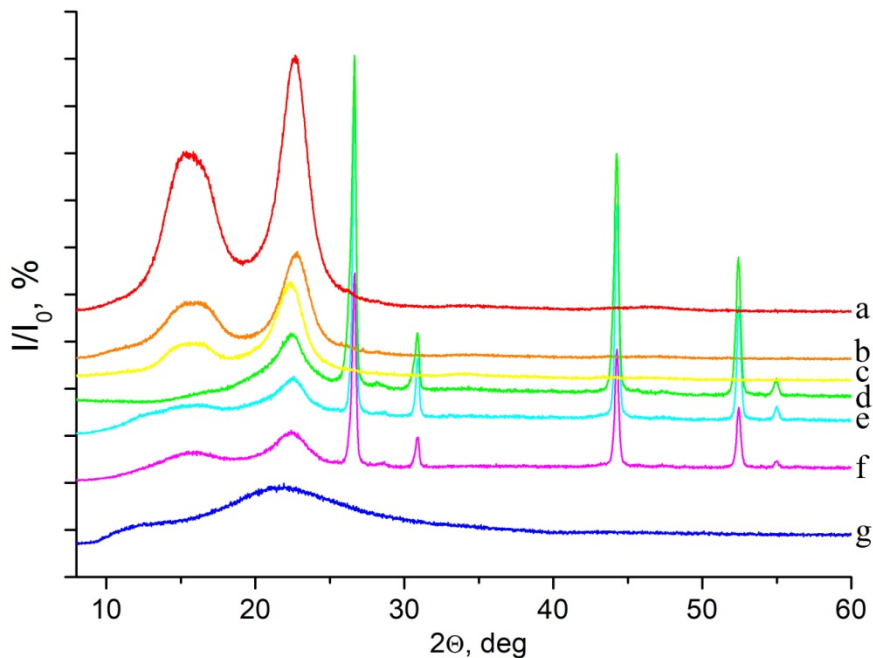
Sample	Particle size (SEM), nm		Particle width (AFM), nm	Average roughness (Ra), nm	Crystallinity index (IC), %
	width	length			
TOCNF	20 ± 6	809 ± 98	19 ± 5	3	78.2
CNC	14 ± 4	107 ± 38	13 ± 3	11	84.6
TOCNF-APS _{7.0}	27±6	818 ± 107	27 ± 5	47	72.2
TOCNF-bAPS _{7.0}	25±7	n.d.*	25 ± 7	16	73.7

318

*No data

319

320 TOCNF-APS_{7.0} films consisted of thickened well-distinguishable nanofibrils (width up to 27±6
 321 nm). Size increase of fibrils is apparently due to their coating with linear polysiloxane network
 322 (Fig. 1c), whereas the nanofibrils in TOCNF-bAPS_{7.0} had their width decreased down to 25±7
 323 nm and exhibited the tendency to glue to each other (Fig. 1d). AFM images of the TOCNF-
 324 bAPS_{7.0} surfaces show 3D siloxane “islands” formed as a result of self-condensation of the
 325 hydrolyzed APS (Fig. 1d, inset). EDX results showed more uniform distribution of elements
 326 (6.4±0.1 at. % Si, 6.8±0.1 at. % N) in TOCNF-APS_{7.0} film compared to the similar data for
 327 TOCNF-bAPS_{7.0} film (6.3±0.4 at. % Si and 6.8±0.4 at. % N, respectively; Figs. S2 and S3). Si/N
 328 ratio in the modified films was close to the same ratio for APS molecules. X-ray diffraction
 329 pattern of TOCNF film contained diffraction peaks at 2θ = 22.5° and 2θ = 14.8–16.8° (double
 330 peak) that corresponded to the (200), (1ī0) and (110) crystallographic planes of monoclinic Iβ
 331 cellulose (Jiang et al., 2013) (78.2% crystallinity degree; Fig. 2a). X-ray diffraction study of
 332 TOCNF-bAPS_{7.0} и TOCNF-APS_{7.0} films did not show any essential changes in their TOCNF
 333 crystal structure after modification: whereas line intensities changed, the diffraction angles
 334 remained the same as for the starting TOCNF films (Figs. 2b, c). Changes in amorphous halo
 335 could be explained by amorphous character of APS attached to TOCNF. The same explanation
 336 could also be given for the crystallinity degree decrease in TOCNF-bAPS_{7.0} and TOCNF-APS_{7.0}
 337 films (Table 1).

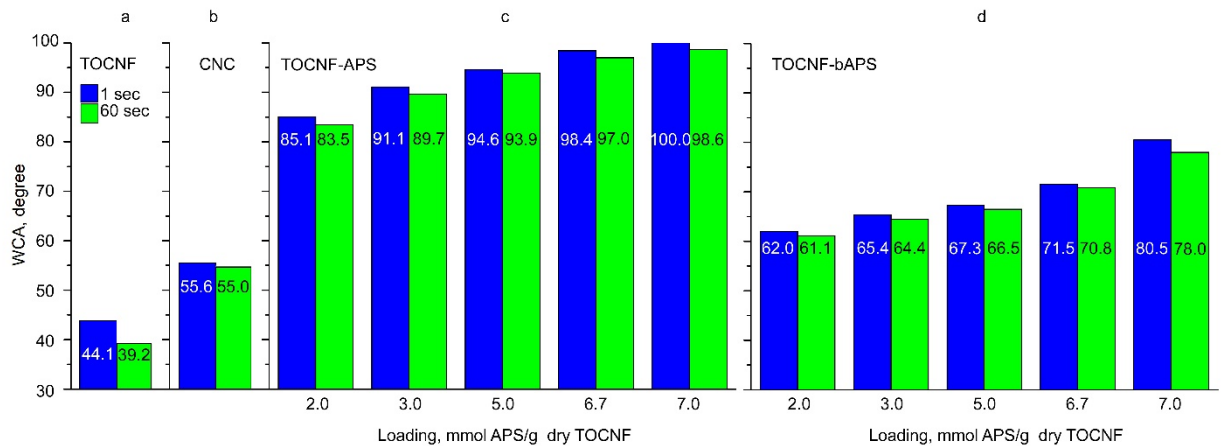


338 **Fig. 2** XRD patterns of the films after the thermal treatment at 105°C: TOCNF (a), TOCNF-
 339 bAPS_{7.0} (b); TOCNF-APS_{7.0} (c), TOCNF:3.5Ho (d), TOCNF:3.5Ho-bAPS_{7.0} (e), TOCNF:3.5Ho-
 340 APS_{7.0} (f), and of APS after thermal treatment at 700°C (g)

342

343 Positions of X-ray diffraction peak maxima of Iβ cellulose in X-ray diffraction patterns remained
 344 the same in the modified composites and TOCNF films (Figs. 2d-f). Some changes in the
 345 diffraction lines intensities could be attributed to the presence of fluorite phase in the studied
 346 specimens. The cubic unit cell parameters of the fluorite phases of the same Sr_{0.92}Ho_{0.08}F_{2.08}
 347 composition, $a = 5.784(1)$ Å, calculated from X-ray diffraction patterns of TOCNF:3.5Ho,
 348 TOCNF:3.5Ho-bAPS_{7.0} и TOCNF:3.5Ho-APS_{7.0} films, corresponded to the similar data for the
 349 starting Sr_{0.92}Ho_{0.08}F_{2.08} powder annealed at 750°C and used in the preparation of the
 350 aforementioned films. In other words, one may conclude that cellulose crystal structure as well
 351 as crystal structure and crystal lattice parameters of up-conversion powders remained unchanged
 352 in the course of the composite films preparation, i.e., only TOCNF surface underwent chemical
 353 transformations.

354 Correlations between water contact angles (WCA) of TOCNF-APS and TOCNF-bAPS films
 355 after thermal treatment at 105°C, depending on the water droplet contact time, and APS loading
 356 are presented in Fig. 3. TOCNF films are more hydrophilic than CNC films: WCAs of TOCNF
 357 films decreased by 4.9° in 60 seconds, whereas WCAs of CNC changed only by 0.43° (Figs. 3a,
 358 b). Such difference in the films properties could be explained by the difference in the chemical
 359 compositions and structures of the films as well as their surface roughness (Wenzel 1936): the
 360 mean surface roughness value (Ra) for TOCNF, estimated by AFM, was more than three times
 361 lower than Ra for CNC (Table 1; Figs. S4a, b). TOCNF-APS films became hydrophobic for APS
 362 loading of 3.0-7.0 mmol/g (film surface was considered hydrophobic when WCA>90° (Li et al.
 363 2007), and hydrophobicity increased when APS loading grew up (Fig. 3c). The films retained
 364 their hydrophobicity when water droplet contact time was increased up to 60 seconds, because of
 365 insignificant (about 1.4°) decrease of WCA. Hydrophilicity of TOCNF-bAPS films significantly
 366 decreased after modification, but, in contrast with TOCNF-APS, TOCNF-bAPS films did not
 367 become hydrophobic even for the maximum APS loading (Fig. 3d). TOCNF-APS_{7.0} and
 368 TOCNF-bAPS_{7.0} films exhibited an increased roughness compared to the starting TOCNF
 369 roughness (Table 1). Ra of TOCNF-APS_{7.0} films showed the highest value and exceeded Ra of
 370 TOCNF-bAPS_{7.0} by factor of about 2 (Table 1; Figs. S4c, d).



371 **Fig. 3** Correlation between the WCA for different nanocellulose films and the water droplet
 372 contact time
 373

374
 375 Hydrophobic properties of the modified composite films can be illustrated by WCA changes
 376 depending from APS loading and the preparation protocol (1 or 2), Table 2. WCAs for the heat-
 377 treated at 105°C composite films were measured in 60 s after applications of water drops on the
 378 surfaces of the films. Unmodified TOCNF:Ho films were hydrophilic with WCAs equal to 39-
 379 44° ($\pm 3^\circ$). The increase of APS loading from 3 to 6 mmol/g TOCNF led to WCA increase from
 380 $90 \pm 2^\circ$ to $101 \pm 2^\circ$ for TOCNF:Ho-APS films. The further increase of APS loading up to 7
 381 mmol/g TOCNF did not affect WCA values for the synthesized TOCNF:Ho-APS films. After
 382 their modification, TOCNF:Ho-APS films became hydrophobic similarly to the changes in
 383 TOCNF-APS hydrophobicity (Fig. 3c). TOCNF:Ho-bAPS films remained hydrophilic even after
 384 the increase of APS loading up to 7 mmol/g TOCNF ($82 \pm 2^\circ$ WCA) as well as TOCNF-bAPS
 385 films (Fig. 3d). We analyzed roughness of the manufactured composite films by AFM technique:
 386 Ra increased from 11 nm for TOCNF:3.5Ho (WCA $44 \pm 3^\circ$) to 16 and 42 nm for the modified
 387 composite TOCNF:3.5Ho-bAPS_{7.0} (WCA $82 \pm 2^\circ$) and TOCNF:3.5Ho-APS_{7.0} (WCA $101 \pm 2^\circ$)
 388 films, respectively (Fig. S5a-c). Just for comparison, WCA and Ra of CNC:5.5Ho film, obtained
 389 according to previously reported technique (Fedorov et al. 2019), were equal to $67 \pm 2^\circ$ (Table
 390 2) and 16 nm (Fig. S5d), respectively. Presumably, WCA values were affected not only by the
 391 chemical modifications, but by the increase of the film surface roughness, too.

392

393 **Table 2** The effect of APS loading on water contact angle and transmittance coefficient of
 394 TOCNF:Ho-APS composite films

Sample	Film composition	Ho content*, wt. %	WCA, (deg)	Transmittance at 650 nm (%)
TOCNF:3.3Ho	TOCNF:3.3Ho (27.1 wt.% Sr _{0.90} Ho _{0.10} F _{2.10})	3.27 ± 0.09	40 ± 3	23.6
TOCNF:3.3Ho-APS _{3.0}	TOCNF:3.3Ho-APS _{3.0} (27.1 wt.% Sr _{0.90} Ho _{0.10} F _{2.10})	3.25 ± 0.09	90 ± 2	23.5
TOCNF:3.3Ho-APS _{5.0}	TOCNF:3.3Ho-APS _{5.0} (27.1 wt.% Sr _{0.90} Ho _{0.10} F _{2.10})	3.26 ± 0.09	96 ± 2	21.4
TOCNF:3.3Ho-APS _{6.7}	TOCNF:3.3Ho-APS _{6.7} (27.1 wt.% Sr _{0.90} Ho _{0.10} F _{2.10})	3.25 ± 0.09	101 ± 2	19.1
TOCNF:3.3Ho-bAPS _{6.7}	TOCNF:3.3Ho-bAPS _{6.7} (27.1 wt.% Sr _{0.90} Ho _{0.10} F _{2.10})	3.24 ± 0.09	82 ± 2	-
TOCNF:3.5Ho	TOCNF:3.5Ho (35.2 wt.% Sr _{0.92} Ho _{0.08} F _{2.08})	3.47 ± 0.10	44 ± 3	20.0
TOCNF:3.5Ho-APS _{5.0}	TOCNF:3.5Ho-APS _{5.0} (35.2 wt.% Sr _{0.92} Ho _{0.08} F _{2.08})	3.46 ± 0.12	97 ± 2	18.5
TOCNF:3.5Ho-APS _{7.0}	TOCNF:3.5Ho-APS _{7.0} (35.2 wt.% Sr _{0.92} Ho _{0.08} F _{2.08})	3.45 ± 0.10	101 ± 2	15.7
TOCNF:3.5Ho-bAPS _{7.0}	TOCNF:3.5Ho-bAPS _{7.0} (35.2 wt.% Sr _{0.92} Ho _{0.08} F _{2.08})	3.45 ± 0.10	82 ± 2	-
TOCNF:4.9Ho	TOCNF:4.9Ho (40.1 wt.% Sr _{0.90} Ho _{0.10} F _{2.10})	4.87 ± 0.14	-	17.2
TOCNF:4.9Ho-APS _{5.5}	TOCNF:4.9Ho-APS _{5.5} (40.1 wt.% Sr _{0.90} Ho _{0.10} F _{2.10})	4.86 ± 0.14	98 ± 2	15.4
TOCNF:5.5Ho	TOCNF:5.5Ho (45.0 wt.% Sr _{0.90} Ho _{0.10} F _{2.10})	5.46 ± 0.15	-	12.3
TOCNF:5.5Ho-APS _{6.0}	TOCNF:5.5Ho-APS _{6.0} (45.0 wt.% Sr _{0.90} Ho _{0.10} F _{2.10})	5.45 ± 0.15	101 ± 2	8.7
CNC:5.5Ho	CNC:5.5Ho** (45.0 wt.% Sr _{0.90} Ho _{0.10} F _{2.10})	-	67 ± 2	22.0
TOCNF:4.9Ho-AKD ₃₀	TOCNF:4.9Ho-AKD ₃₀ *** (40.0 wt.% Sr _{0.90} Ho _{0.10} F _{2.10})	-	123 ± 2	11.3

395 * Ho content was determined by chemical analysis (see Supplementary Information method SM2)

396 ** (Fedorov et al. 2019)

397 *** (Fedorov et al. 2020)

398

399 Earlier (Fedorov et al. 2019), we have shown that formation of hydrogen bonds between F⁻ ions
 400 from SrF₂:Ho and OH⁻ moieties from nanocellulose was the key factor determining dispersion
 401 stability. Semitransparent bluish dispersions, formed at 1.10 wt.% TOCNF, 0.70 wt.% APS and
 402 0.2 wt.% SrF₂:Ho concentrations, were stable for at least 5-day periods (Figs. S1i-j). Increase in
 403 APS concentration up to 1.27 wt.% and SrF₂:Ho concentration up to 1.27 wt.% resulted in
 404 formation of viscous opaque TOCNF:Ho-bAPS gels (Fig. S1k). Opaque TOCNF:Ho-APS
 405 dispersions, stable for the same 5-day period, were formed under the similar conditions without
 406 any signs of flocculation or sedimentation (Fig. S1 l): stability of TOCNF:Ho-APS dispersions
 407 was the key factor for the homogeneous distribution of the up-converting particles in the
 408 synthesized films casted from solutions.

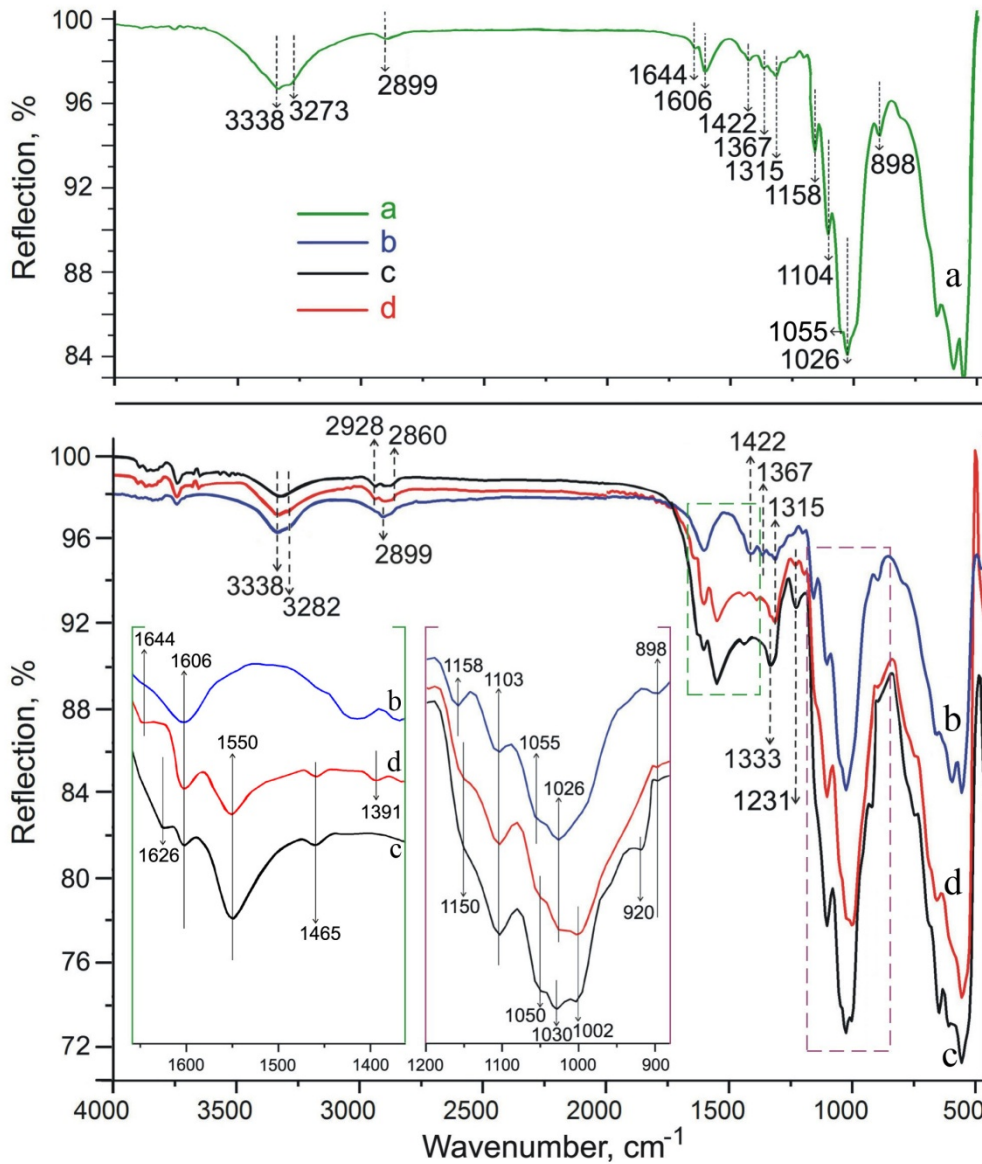
409 Analysis of experimental results obtained confirmed the influence of film modification on the
 410 morphology and wettability of TOCNF surfaces: TOCNF-APS and TOCNF:Ho-APS acquired
 411 hydrophobicity in contrast with TOCNF-bAPS and TOCNF:Ho-bAPS films.

412

413 Characterization of chemical structures and thermal properties of TOCNF/SrF₂:Ho-APS и
 414 TOCNF/SrF₂:Ho-bAPS composite films

415
416
417

FTIR-spectra of unmodified and modified composite films after their thermal treatment at 105°C are presented in Fig. 4.

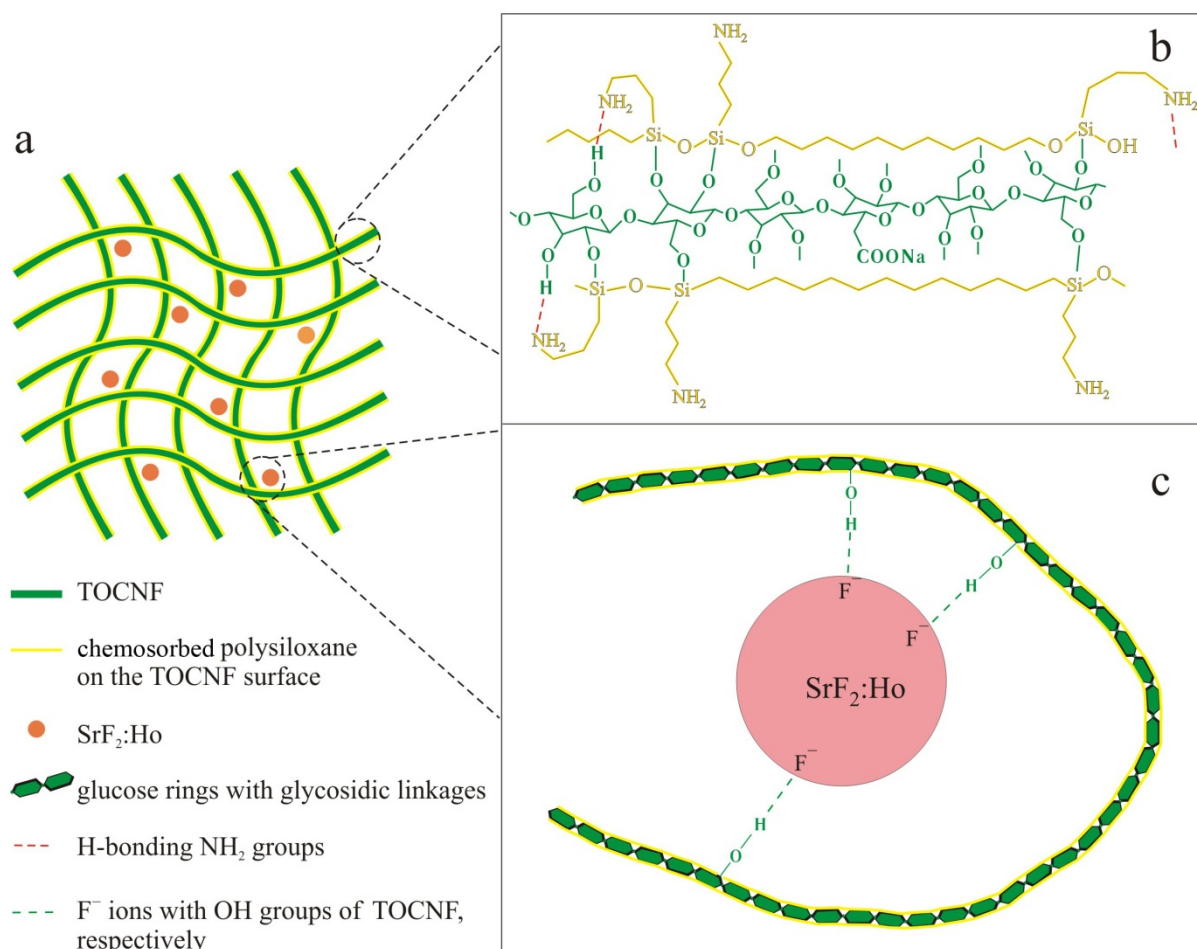


418
419
420
421

Fig. 4 FTIR-spectra of TOCNF (a), TOCNF:3.5Ho (b), TOCNF:3.5Ho-APS_{7.0} (c), and TOCNF:3.5Ho-bAPS_{7.0} (d) films after their thermal treatment at 105°C

422 FTIR-spectrum of TOCNF comprises absorption bands typical for cellulose macromolecules
423 (Fig. 4a): bands at 3273-3338 (wide), 2899 and 1644 cm⁻¹ have been assigned to the stretching
424 vibration of O-H hydrogen bond, C-H stretching, OH bending of the absorbed water vibrations,
425 respectively. Three bands at 1422 cm⁻¹, 1367 cm⁻¹ and 1315 cm⁻¹ are associated with cellulose
426 parent chain. 1158 cm⁻¹ band corresponds to the asymmetric bridge C-O-C stretching. 1104 cm⁻¹
427 band corresponds to the asymmetric ring stretching. 1055 and 1026 cm⁻¹ bands are related with
428 C-O-C pyranose ring skeletal vibrations. A small sharp band at 898 cm⁻¹ is attributed to the β-
429 glycosidic linkages between the anhydroglucose rings in the cellulose (Chen et al. 2016; Liang
430 and Marchessault 1959; Oh et al. 2005). The band at 1606 cm⁻¹ corresponds to COO⁻ stretching
431 in sodium form (Jiang et al. 2013). The FTIR spectrum of TOCNF:3.5Ho composite film (Fig.
432 4b) is similar to that of TOCNF except for a small shift from 3273 cm⁻¹ to 3282 cm⁻¹ of
433 3282-3338 cm⁻¹ band for the composite film; this confirms the formation of interfacial hydrogen
434 bonds between F⁻ ions of the up-conversion particles and OH groups of TOCNF (Fedorov et al.
435 2019).

436 Modification of TOCNF:3.5Ho-APS_{7.0} film resulted in appearance of additional adsorption
437 bands in FTIR spectrum (Fig. 4c): two weak bands at 2928 cm⁻¹ and 2860 cm⁻¹ corresponded to
438 asymmetric and symmetric stretching of CH₂ fragment of APS aminopropyl groups (Kim et al.
439 2011; Masmoudi et al. 2013); strong 1550 cm⁻¹ band corresponded to N–H bending vibration of
440 primary amine groups (Khanjanzadeh et al. 2018; Robles et al. 2018); and weak 1626 cm⁻¹ band
441 corresponded to the deformation mode of the NH₂ groups that are hydrogen-bonded to the OH
442 groups of cellulose. Such band assignment is in an agreement with previously reported data
443 regarding treatment of SiO₂ and copper surfaces with APS (Culler et al. 1985, Masmoudi et al.
444 2013). The presence of 1606 cm⁻¹ band (COO⁻Na⁺) allowed us to assume that non-oxidized
445 primary and secondary OH groups took part in the condensation reaction, whereas oxidized C6
446 primary hydroxyls did not participate in the latter process. Also, 1333 cm⁻¹ and 1231 cm⁻¹ bands
447 corresponded to C–N bond bending modes (Hokkanen et al. 2014); and 1465 cm⁻¹ weak bend
448 corresponded to CH₂ bending of the aminopropyl groups (Ishida et al. 1982; Pavia et al. 2009).
449 The absence of 1575 cm⁻¹ and 1485 cm⁻¹ absorption bands, corresponding to the vibrational
450 modes of bicarbonated amino groups associated with atmospheric water and carbon dioxide
451 confirmed removal of moisture and CO₂ after the thermal treatment at 105°C followed by drying
452 in the desiccator (Kim et al. 2011). Essential intensity increase of the bands within 1000-1150
453 cm⁻¹ indicated formation of Si–O–Si siloxane bonds and covalent Si–O–C_{cellulose} bonding.
454 However, overlapping of strong absorption bands, corresponding to C–O–C stretching and
455 pyranose ring skeletal vibrations of cellulose, prevented the unequivocal identification of the
456 typical Si–O–Si и Si–O–C_{cellulose} bonds giving absorption bands in the same spectrum range.
457 According to the previous reports (Masmoudi et al. 2013; Vandenberg 1991), the presence of
458 Si–O–Si absorption band at the higher frequencies (ca. 1148 cm⁻¹ and above) was caused by
459 formation of the three dimensional siloxane units, while lower frequency band (1034-1050 cm⁻¹)
460 indicated formation of long linear Si–O–Si chains, and 1000-1012 cm⁻¹ bands pointed out at the
461 very low degree of self-condensation. Thus, appearance of the new absorption band at 1002 cm⁻¹
462 in the TOCNF:3.8Ho-APS_{7.0} spectrum, shift of the other band from 1055 cm⁻¹ to 1050 cm⁻¹
463 along with its intensity increase confirmed formation of linear Si–O–Si chains with various
464 degree of condensation (chain length). Shift of 1028 cm⁻¹ band up to 1030 cm⁻¹ was caused by
465 Si–O–Si linear self-condensation and covalent Si–O–C_{cellulose} bonding (Rachini et al. 2012).
466 Very low intensity of 920 cm⁻¹ band, corresponding to Si–O stretching, indicated an
467 insignificant content of Si–OH groups (Masmoudi et al. 2013). The latter observation, as well as
468 ethoxy group absence, is in agreement with literature data (Beari et al. 2001, Salon et al. 2007,
469 Salon et al. 2010) that lowering pH down to 4.0-4.5 promoted APS hydrolysis and delayed Si–
470 OH self-condensation (Fig. S6). TOCNF:3.8Ho-bAPS_{7.0} spectrum (Fig. 4d) differed from the
471 one of TOCNF:3.8Ho-APS_{7.0} by the absence of 1626 cm⁻¹ and appearance of 1644 cm⁻¹ weak
472 absorption band, corresponding to the bending vibrations of adsorbed water molecules (Fedorov
473 et al. 2019), and 1391 cm⁻¹ absorption band, corresponding to deformation vibrations of CH₃
474 methoxy groups from -O-CH₂CH₃ moieties (Kim et al. 2011). Intensity increase of 1150 cm⁻¹
475 weak band and the absence of 1030 cm⁻¹ in TOCNF:3.5Ho-bAPS_{7.0} film spectrum confirmed the
476 formation of the three-dimensional siloxane units along with linear oligomers. Analysis of FTIR
477 spectrum of the thermally treated at 105°C TOCNF:3.5Ho-APS_{7.0} film confirmed the presence of
478 the linear APS oligomers and formation Si–O–C_{cellulose} covalent bonds as a result of the
479 condensation with TOCNF hydroxyls. Ethoxy group presence in TOCNF:3.5Ho-bAPS_{7.0} films
480 indicated the presence of physically adsorbed unhydrolyzed APS.
481 Both primary and secondary hydroxyl groups of cellulose can participate in the silylation
482 reaction (Pereira et al. 2020), whereas, in TEMPO oxidation, only primary hydroxyls can
483 undergo chemical transformations. Schematic structure of TOCNF:Ho-APS films is presented in
484 Fig. 5.

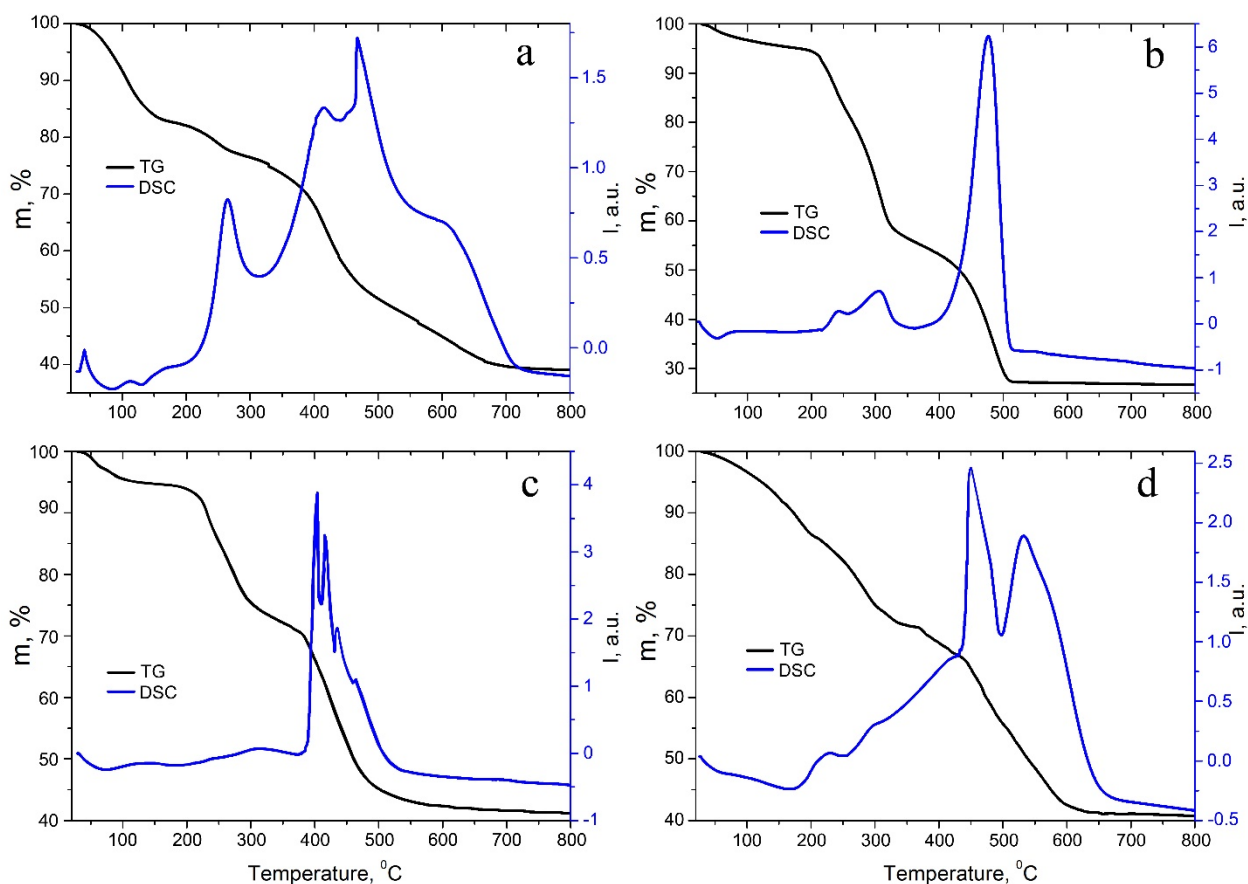


485
 486 **Fig. 5** Mechanisms of the composite TOCNF:Ho-APS film formation: schematic representation
 487 of TOCNF:Ho-APS film structure (a); linear polysiloxane, bound to TOCNF by Si-O-C covalent
 488 bond, with chemisorbed polysiloxane (b); hydrogen bonds between TOCNF and SrF₂:Ho (c)
 489

490 Our studies have shown that pH value of the first step of the silylation in aqueous medium
 491 significantly affected hydrophobic properties of the modified composite APS films. The higher
 492 WCA values of TOCNF:Ho-APS films, compared to the similar data for TOCNF:Ho-bAPS
 493 films, has been confirmed by the results of FTIR spectroscopy. Perhaps, hydrophobicity of
 494 TOCNF:Ho-APS films was caused by evenly distributed layer of chemisorbed linear
 495 polysiloxane and hydrogen bonds between NH₂ moieties of aminopropyl groups and OH groups
 496 of TOCNF. The latter bonds changed the APS configuration at the film surface: aminopropyl
 497 groups were bent, and their polar NH₂ moieties were oriented toward TOCNF surfaces, whereas
 498 propyl fragments were oriented along the surface (Culler et al. 1985; Indarti et al. 2019;
 499 Masmoudi et al. 2013; Rachini et al. 2012).

500 According to TGA data, solid APS, obtained by drying under air at 25°C and further annealing at
 501 105°C (see Supplementary Information, method SM1), lost about 16.4% of its weight at 150 °C
 502 (Fig. 6a). DSC curve comprised endo-effects at 84°C and 131 °C, corresponding to the
 503 evaporation of ethanol formed during the hydrolysis of residual APS, as well as adsorbed water.
 504 The further heating at 150–270°C caused the additional weight loss of 5.8% and it was
 505 accompanied with the exo-effect at 265°C corresponding to the evaporation of water, formed in
 506 the course of the self-condensation process and Si—O—Si bond formation, and to the oxidation of
 507 amino groups to imino-groups. Heating at 270–700°C caused additional 38% weight loss, and it
 508 was accompanied by the three exo-effects at 416°C, 470°C and 606°C associated with
 509 aminopropyl group oxidation, oxidative thermal decomposition with Si—O—Si bond cleavage
 510 and oxidation of residual carbon (Peña-Alonso et al. 2005; Qiao et al. 2015). The residue after

511 700°C annealing was about 39.8% of the initial weight. EDX analysis of this residue indicated
 512 the presence of O and Si only with O:Si ratio being to 2:1 (Fig. S7). XRD has confirmed that the
 513 residue was single-phase amorphous SiO₂ (Fig. 2g).



514 **Fig. 6** TG and DSC curves for APS (a) and TOCNF:3.3Ho (b), TOCNF:3.3Ho-APS_{6.7} (c),
 515 TOCNF:3.3Ho-bAPS_{6.7} (d) composite films after drying at 105°C
 516

517
 518 According to TGA and DSC data, onset thermal degradation (T_{onset}) of TOCNF:3.3Ho and
 519 TOCNF:3.3Ho-APS_{6.7} films under air started at 204°C and 216°C, respectively (Figs. 6b and
 520 6c). At the first step (25–150°C), TOCNF:3.3Ho film demonstrated only a little weight loss
 521 (about 4.4%) because of evaporation of adsorbed water (Fig. 6b). The higher weight loss for
 522 TOCNF:3.3Ho-APS_{6.7} film (about 5.7%) was caused by additional water evaporation produced
 523 by the condensation of remaining silanol groups (Fig. 6c). The weight loss of TOCNF:3.3Ho
 524 film was about 39% in the 150–330°C temperature range. It was accompanied by two
 525 exothermic effects in DSC curve at 240°C and 304°C (Fig. 6b), that corresponded to the thermal
 526 degradation of cellulose due to decarboxylation of TOCNF, depolymerization and cleavage of
 527 glycosidic linkages of cellulose (Fukuzumi et al. 2010; Lichtenstein and Lavoine 2017). The
 528 third exothermic effect at 472°C was due to the residual carbon oxidation. The weight loss of
 529 TOCNF:3.3Ho film at the third stage of decomposition (330–510°C) was about 29.5%.
 530 According to TGA, the residue weight after the decomposition of TOCNF:3.3Ho film under air
 531 was 27.1%, which corresponds to the initial content of up-conversion powder in the composite
 532 film (as confirmed by quantitative chemical analysis for holmium content, Table 2).
 533 For TOCNF:3.3Ho-APS_{6.7} film, TGA study showed 23.4% weight loss in 150–380°C
 534 temperature range (Fig. 6c). The weight loss in this temperature range was multi-stage, and it
 535 was accompanied by several exothermic effects in DSC curve, which occurred almost
 536 simultaneously. These complicated processes corresponded to the oxidative destruction of
 537 cellulose and amino-group oxidation with imino-group formation. The further 29.9% weight loss
 538 of TOCNF:3.3Ho-APS_{6.7} film at 380–650°C proceeded in a multi-step manner and was

539 accompanied with four exothermal effects at 406, 416, 440 and 468°C, which were related to the
540 aminopropyl group oxidation, Si—O—Si bond cleavage and oxidation of residual carbon.
541 According to TGA, the residue weight after the decomposition of TOCNF:3.3Ho-APS_{6.7} film
542 under air was 41.3%, which included Sr_{0.90}Ho_{0.10}F_{2.10} and SiO₂. EDX analysis of residue
543 indicated the presence of oxygen and silicon (O:Si = 2:1 ratio) (Fig. S7). The holmium content in
544 TOCNF:3.3Ho-APS_{6.7} film was 3.25 ± 0.09 wt.% as determined by quantitative chemical
545 analysis (Table 2), which corresponded to the initial 27.1 wt.% content of Sr_{0.90}Ho_{0.10}F_{2.10}
546 powder in the composite film. The difference between the residue after the decomposition of
547 TOCNF:3.3Ho-APS_{6.7} film (41.3%) and the content of Sr_{0.90}Ho_{0.10}F_{2.10} powder in the composite
548 film (27.1%) was 14.2% and corresponded to SiO₂ content of the residue after the said film
549 decomposition. The value of 14.2% SiO₂ corresponded to its theoretical content calculated on the
550 basis of the initial APS loading during the preparation of the composite film (the theoretical
551 calculation took into account the drying loss of APS at 105 °C; (see Supplementary Information,
552 method SM1).

553 TGA data for TOCNF:3.3Ho-bAPS_{6.7} film decomposition included 7.4% weight loss at 150°C
554 (Fig. 6d) and 4.6% at 150–200 °C (i.e., 12.0% weight loss at 200 °C). Endo-effect at 173°C
555 corresponded to the evaporation of ethanol, formed in the course of hydrolysis of remaining
556 APS, adsorbed water and physically adsorbed APS (Peña-Alonso et al. 2005; Qiao et al. 2015).
557 TOCNF:3.3Ho-bAPS_{6.7} film lost 19.7% weight at 200–380°C. Two exothermal effects at 232°C
558 and 300°C were attributed to the beginning of cellulose oxidative destruction and amino-group
559 oxidation with imino-group formation. The thermal decomposition of TOCNF:3.3Ho-bAPS_{6.7}
560 film started at about T_{onset} of 200°C. Weight loss of TOCNF:3.3Ho-bAPS_{6.7} film at 380–650°C
561 (27.1%) was accompanied by two exo-effects at 450°C and 536°C related to aminopropyl group
562 oxidation, -Si—O—Si- bond cleavage and residual carbon oxidation. According to the TGA data,
563 the residue after thermal decomposition of TOCNF:3.3Ho-bAPS_{6.7} film (41.2%) comprised
564 Sr_{0.90}Ho_{0.10}F_{2.10} and SiO₂. 3.24 ± 0.09 wt.% holmium content (chemical analysis data)
565 corresponded to the initial content of Sr_{0.90}Ho_{0.10}F_{2.10} powder (27.1 wt.%, Table 2); and 14.1
566 wt.% difference corresponded to SiO₂.

567 Thus, TGA/DSC data confirmed an increase in the thermal stability of TOCNF:3.3Ho-APS_{6.7}
568 modified film compared to the thermal stability of the unmodified film. TOCNF:Ho-APS films
569 have also shown the higher thermal stability (T_{onset} 216°C) and hydrophobicity (WCA 101 ± 2°).
570 The said increase in thermal stability of TOCNF:Ho-APS films was caused by the formation of
571 Si—O—C_{cellulose} covalent bonds with the surface OH groups of TOCNF as well as the presence of
572 homogeneous coating with linear APS oligomer network.

573

574 Optical properties and morphology of TOCNF:Ho-APS composite films

575

576 Transparent and flexible TOCNF, TOCNF-APS_{3.0} и TOCNF-APS_{7.0} films were obtained without
577 cracks (Figs. 7a-c). Their transmittance coefficients at 650 nm were 89.4%, 70.0% and 61.9%,
578 respectively (Figs. 8 a-c); transmittance coefficients decreased with the increase in APS loading.



579 **Fig. 7** Appearance of the films: TOCNF (a), TOCNF-APS_{3.0} (b), TOCNF-APS_{7.0} (c)
 581 TOCNF:3.3Ho (d), TOCNF:3.5Ho (e), TOCNF:5.5 Ho (f), TOCNF:3.3Ho-APS_{3.0} (g),
 582 TOCNF:3.5Ho-APS_{7.0} (h), TOCNF:5.5Ho-APS_{6.0} (i)

583
 584 The transmittance coefficients of the films depended on both the APS loading and the content of
 585 the up-conversion powder (Table 2). Comparison of the transmission spectra of the composite
 586 films with the same content of up-conversion powder (27.1 wt.% Sr_{0.90}Ho_{0.10}F_{2.10})
 587 TOCNF:3.3Ho and TOCNF:3.3Ho-APS_{3.0} at a loading of 3.0 mmol APS per 1 g of dried
 588 TOCNF showed that the decrease in transmittance was mainly due to the upconversion powder
 589 content (Figs. 8d, e).

590 The further increase of APS content exhibited the more explicit effect on the film transmission
 591 spectra. Comparison of the transmission spectra of the composite TOCNF:3.5Ho and
 592 TOCNF:3.5Ho-APS_{7.0} films with the same content of up-conversion powder (35.2 wt.%
 593 Sr_{0.92}Ho_{0.08}F_{2.08}) revealed decreasing of the transmittance of modified films decreases with
 594 increasing APS loading (Figs. 8f, g; Table 2). Composite films with an APS loading of 3-7 mg/g
 595 TOCNF were yellowish color, homogeneous, strong, flexible and translucent (Figs. 7g-i).
 596 Content of the up-conversion powder affected the composite film transmittance at higher extent
 597 than the APS loading.

598

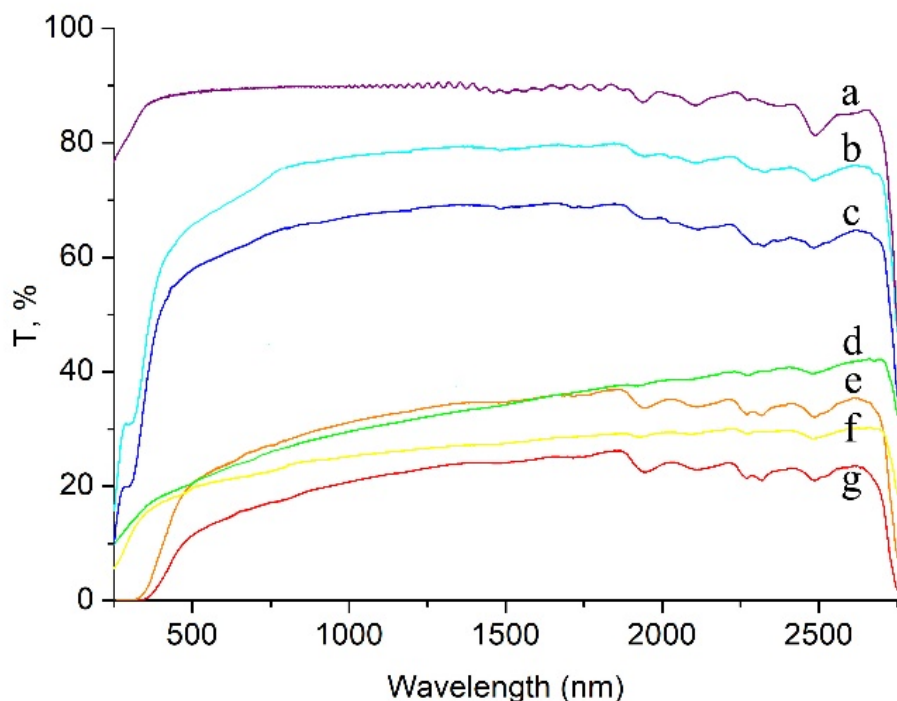
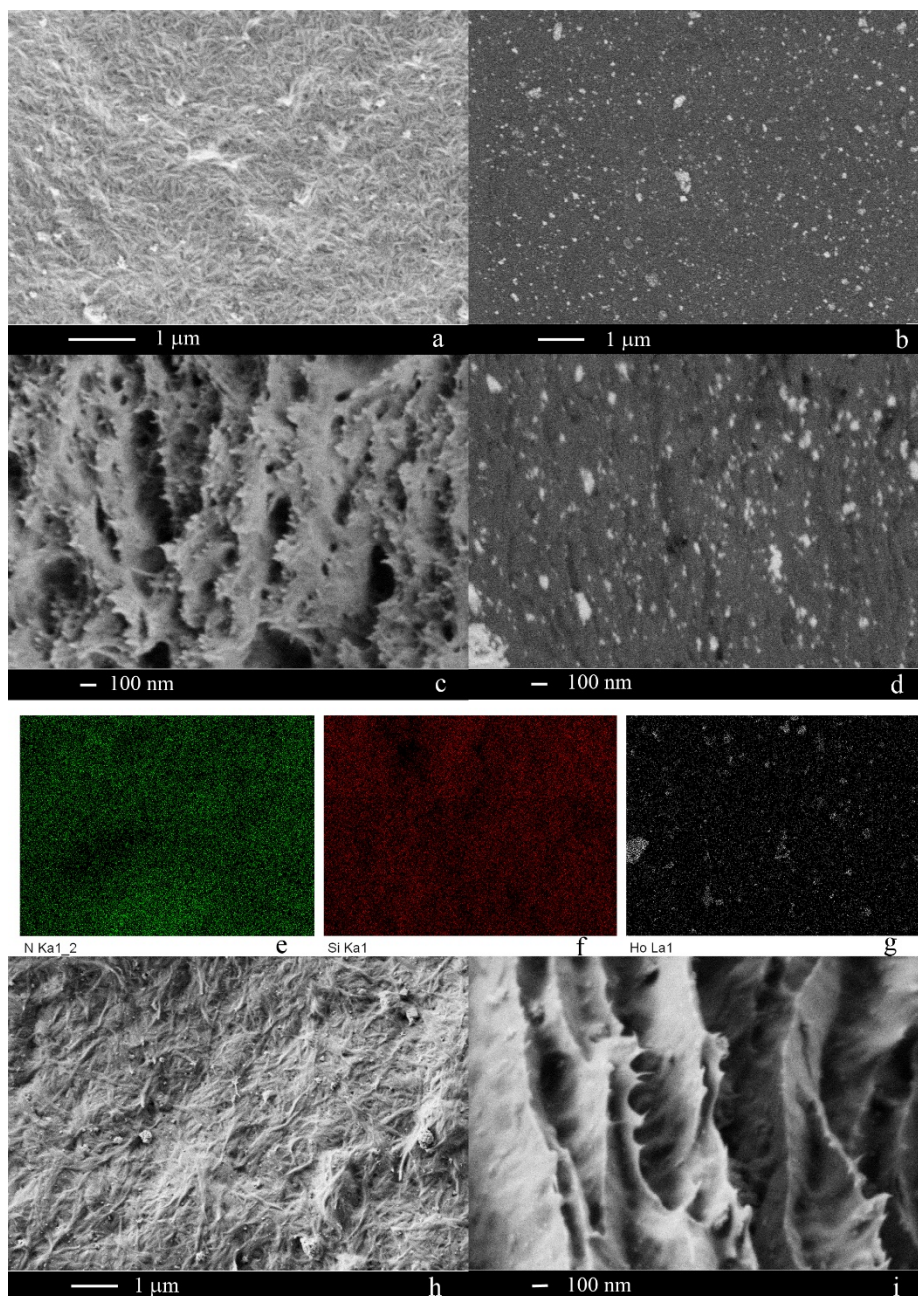


Fig. 8 Transmission spectra of the films: TOCNF (a), TOCNF-APS_{3.0} (b), TOCNF-APS_{7.0} (c) TOCNF:3.3Ho (d), TOCNF:3.3Ho-APS_{3.0} (e), TOCNF:3.5Ho (f), TOCNF:3.5Ho-APS_{7.0} (g)

599
600
601
602
603
604
605
606
607
608
609
610
611
612
613
614
615

The morphology of surface and cross-sections of the films, distribution of up-conversion particles and elements (N, Si) in the hydrophobic nanocomposite TOCNF:Ho-APS films were analyzed by SEM and EDX. Compared to unmodified TOCNF films (20 ± 8 nm nanofibril width, Fig. 1a), TOCNF:3.3Ho-APS_{5.0} films retained the fibrillar structure of TOCNF with thickened nanofibrils (27 ± 7 nm nanofibril width) due to continuous and uniform coverage with a polysiloxane network with up-conversion particles located between fibrils (Fig. 9a). The cross-section of the TOCNF:3.3Ho-APS_{5.0} film had a mesoporous structure with a pore size of 51 ± 20 nm (Fig. 9 c). Cracks on the film cleavage were formed as a result of mechanical action during the film splitting. Samples of the TOCNF:3.3Ho-APS_{5.0} composite film had a homogeneous morphology with uniformly distributed up-conversion particles, which was confirmed by the film surface and the cross-section Z-contrast imaging (Fig. 9 b, d). The size of most up-conversion particles ranged from 30 to 79 nm with a small amount of agglomerates (154 ± 34 nm).



616
 617 **Fig. 9** SEM images and EDX maps of TOCNF:3.3Ho-APS_{5.0} film: surface (a, b); cross-section
 618 (c, d); images in topographic contrast mode (a, c); images in Z-contrast mode (b, d); EDX maps
 619 for N (e), Si (f) and Ho (g) elements distribution across the surface. SEM images of
 620 TOCNF:3.3Ho-bAPS_{5.0} film surface (h) and cross-section (i)

621
 622 The uniformity of N, Si and Ho element distribution in TOCNF:Ho-APS films was confirmed by
 623 elemental mapping (Fig. 9e-g) and EDX analysis (Fig. S8). EDX analysis indicated that the
 624 measured Sr/Ho atomic ratio in the composite films was very close to that measured in
 625 Sr_{0.90}Ho_{0.10}F_{2.10} powder. The EDX results confirmed the presence of N = 4.8 ± 0.2 at.% and Si =
 626 4.7 ± 0.4 at.%.

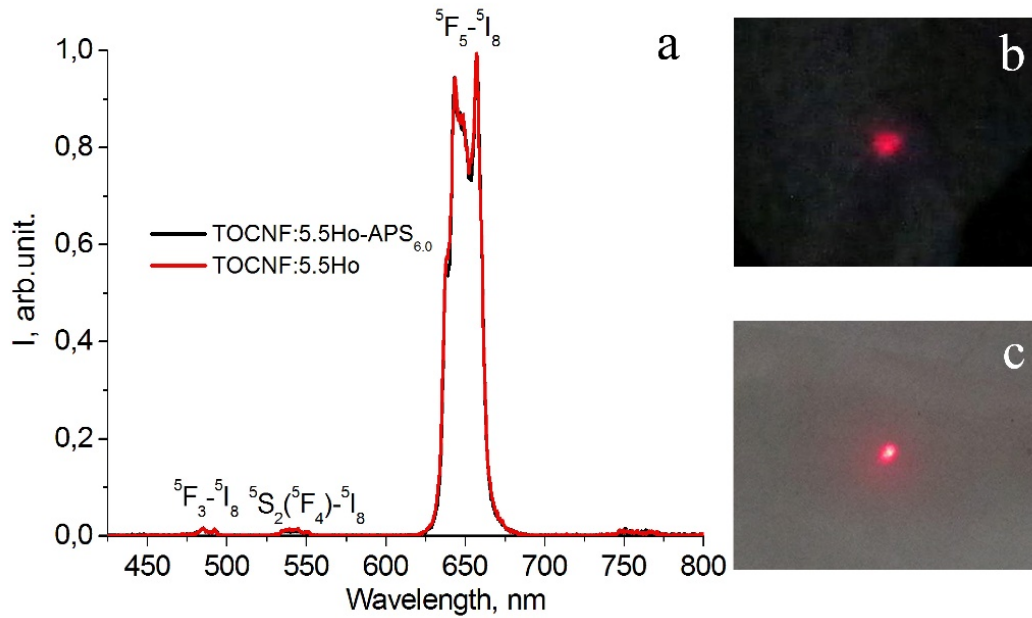
627 The surface morphology and cross-section of TOCNF:3.3Ho-bAPS_{5.0} films are presented in Figs.
 628 9h and 9i for comparison with TOCNF:3.3Ho-APS_{5.0} film. The TOCNF:3.3Ho-bAPS_{5.0} film
 629 surfaces were formed by glued together nanofibrils, 3D siloxane “islands”, and non-hydrolyzed
 630 APS. Cross-sections were formed by dense layers of glued nanofibrils.

631 Composite films TOCNF:Ho-APS with an optimal combination of hydrophobic, optical and
 632 mechanical properties were obtained with an up-conversion powder content of up to 45 wt.% and
 633 an APS loading of 5.0 - 6.0 mmol/g TOCNF.

634
635
636
637
638
639
640

Luminescent properties and laser damage threshold of TOCNF:Ho-APS films

Analysis of the up-conversion luminescence spectra of hydrophobic TOCNF:Ho-APS films and hydrophilic TOCNF:Ho films, heat treated at 105 °C, showed that the films with the same amount of holmium demonstrated similar luminescence intensity (Fig. 10).



641
642
643
644
645
646
647
648
649
650
651
652
653

Fig. 10 Up-conversion luminescence spectra of the composite films (a); and IR light visualization by the composite films: TOCNF:5.5Ho (b), TOCNF:5.5Ho-APS_{6.0} (c). Laser excitation of Ho³⁺ ions ⁵I₇ energy level at a wavelength of 1912 nm, beam diameter 10 μm

The laser damage threshold (LDT) (Wood 2014) as the radiation intensity leading to irreversible changes in the film was determined by visual observation of damage/darkening spots (λ = 1940 nm, beam diameter 1500 μm) for five composite up-conversion films. The 1940 nm wavelength was selected based on the location of the holmium absorption maximum for SrF₂:Ho solid solution (Lyapin et al 2017). The highest laser radiation durability (104.71 W/cm²) was registered for a TOCNF:5.5Ho-APS_{6.0} composite film (Table 3).

Table 3 Laser damage threshold of composite films based on CNC and TOCNF

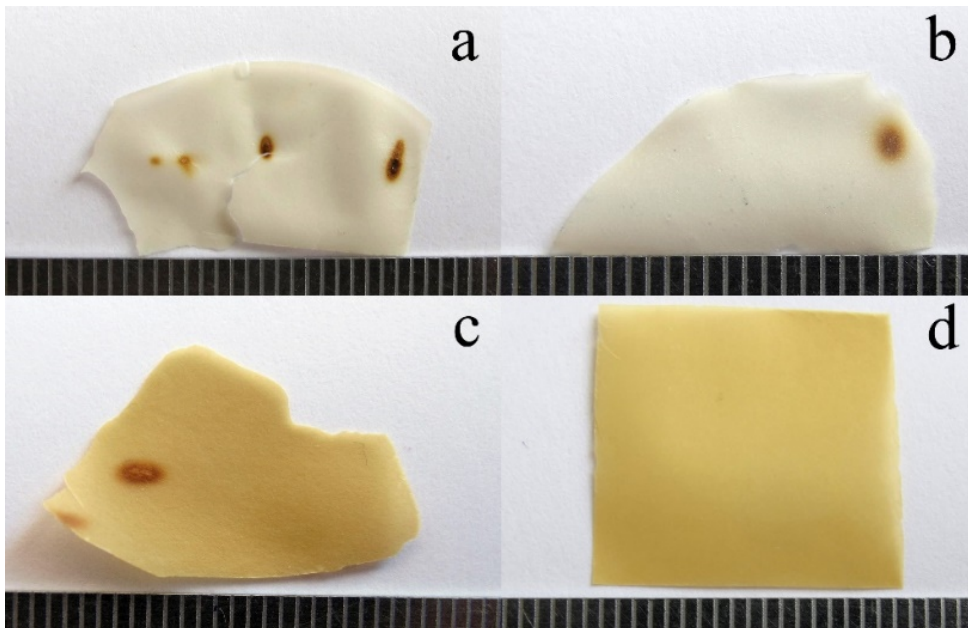
Sample	H ₂ O content determined by drying at 150°C, wt. %	Onset thermal degradation T _{onset} , °C	The power at which the film burns or darkens, W	LDT, W/cm ²	Transmittance at 650 nm (%)
TOCNF:5.5Ho	4.4	204	0.84	47.3	12.3
CNC:5.5Ho	2.3*	157*	0.80	45.3	22.0*
TOCNF:4.9Ho-AKD ₃₀	3.0**	210**	0.95	53.7	11.3**
TOCNF:5.5Ho-bAPS _{6.0}	7.4	200	0.83	47.3	-
TOCNF:5.5Ho-APS _{6.0}	5.7	216	1.85	104.7	8.7
TOCNF-APS _{7.0}	5.7	216	> 3	>168	61.9
TOCNF	4.4	204	1.845	104.4	89.4

654 * (Fedorov et al. 2019)
655 ** (Fedorov et al. 2020)

656
657
658

LDT depends on the optical, mechanical, thermal properties, morphology of the irradiated material, and the presence of absorbing inclusions (Emmert and Rudolph 2014). For materials

659 based on unmodified cellulose, the predominant cause of damage is thermal degradation due to
660 evaporation of moisture and subsequent charring of the films in the illuminated spot (Emmert
661 and Rudolph 2014). For the composite films subjected to 0.84 W irradiation, the damage did not
662 occur only for the TOCNF:5.5Ho-APS_{6.0} film (Fig. 11d).
663



664
665 **Fig. 11** Images of composite films after laser irradiation with a power of 0.84 W: CNC:5.5Ho
666 (a); TOCNF:5.5Ho (b); TOCNF:5.5Ho-bAPS_{6.0} (c); TOCNF:5.5Ho-APS_{6.0} (d)
667

668 The reasons for the lowest laser radiation durability of the CNC:5.5Ho films were the low T_{onset}
669 and the low H_2O content. However, LDT of CNC:5.5Ho films slightly differed from LDTs of
670 TOCNF:5.5Ho and TOCNF:5.5Ho-bAPS_{6.0} films, despite the significant difference in their
671 thermal stability. The difference in surface roughness was not so important because the
672 nanoroughness (measured by AFM) was too little compared to the laser wavelength (1940 nm)
673 to cause significant scattering and absorption of laser radiation. The optical properties of the
674 composite films with the same content of up-conversion particles differed insignificantly (Table
675 3). The highest transmittance coefficient was observed for unmodified TOCNF film (89.4%)
676 with LDT 104.4 W/cm^2 . The highest LDT value of 168 W/cm^2 belonged to modified non-
677 composite TOCNF-APS_{7.0} film. The presence of absorbing $\text{SrF}_2:\text{Ho}$ particles greatly reduces the
678 LDT of composite films. The functionalization of TOCNF films by APS significantly increases
679 their durability to laser radiation.

680 The main factors affecting the LDT value of nanocellulose-based nanocomposite films were the
681 surface morphology, the presence of a uniform amorphous, thermostable coating, and the
682 formation of a mesoporous film structure. As it has been already mentioned, surface of
683 TOCNF:5.0Ho-bAPS_{6.5} films exhibited the tendency to glue nanofibrils to each other and form
684 3D siloxane islands as a result of self-condensation of the hydrolyzed APS, and the film cross-
685 section was formed by layers with a dense structure (Figs. 9h, i). In contrast to these films, on the
686 surface of thickened nanofibrils of the TOCNF:5.5Ho-APS_{6.0} film, a homogeneous polysiloxane
687 layer was formed mainly due to linear oligomers grafted on the TOCNF surface. Mesopores are
688 clearly visible in the film cross-section (Figs. 9a, c). Such a coating has increased resistance to
689 thermal oxidative degradation. A similar phenomenon in the study of laser damage to
690 antireflection SiO_2 coatings was reported earlier (Li et al 2014).

691 Thus, we developed up-conversion hydrophobic nanocomposite TOCNF:Ho-APS films, which
692 possess comparable luminescence intensity to the CNC/ $\text{SrF}_2:\text{Ho}$ and TOCNF: $\text{SrF}_2:\text{Ho}$ -AKD
693 films obtained earlier (Fedorov et al. 2019, 2020), while having the higher resistance to laser
694 radiation.

695

696 **Conclusions**

697

698 In conclusion, we have developed a novel preparation technique of luminescent composite
699 cellulose films. The films were prepared by solution casting technique from precursor dispersion
700 (SrF₂:Ho up-conversion particles in APS-modified aqueous TOCNF solution at pH = 4.0-4.5)
701 followed by the thermal treatment at 105 °C. This technique produced thin (50-60 microns),
702 hydrophobic (WCA = 97±2° – 101±2°), strong, and flexible semitransparent composite
703 TOCNF:Ho-APS films with a uniform distribution of up-conversion particles (30-45 wt.%
704 SrF₂:Ho content, and APS loading of 5.0-6.0 mmol/g dry TOCNF). TOCNF:Ho-APS film
705 hydrophobicity has been caused by evenly distributed layer of chemisorbed linear polysiloxane
706 on TOCNF surface as well as by changed configuration of aminopropyl groups with propyl
707 hydrophobic fragments oriented along the film surface, and NH₂ moieties formed hydrogen
708 bonds with TOCNF free hydroxyls and became oriented away from the external polysiloxane
709 layer. Luminescence intensities of TOCNF:Ho-APS films (Ho³⁺ ⁵I₇ level excitation with 1912
710 nm laser irradiation) coincided with that of CNC/SrF₂:Ho and TOCNF:SrF₂:Ho-AKD films
711 (Fedorov et al. 2019, 2020). The thermal decomposition (216°C) and LDT (104.7 W/cm²) for
712 TOCNF:Ho-APS film were higher than CNC/SrF₂:Ho (157°C; 45.3 W/cm²) and
713 TOCNF:SrF₂:Ho-AKD (210°C; 53.7 W/cm²) films. TOCNF/SrF₂:Ho films are eco-friendly, and
714 they can be used for visualization of 2 μm laser radiation in medicine and long-distance
715 atmosphere monitoring.

716

717 **Declarations**

718

719 **Compliance with ethical standards**

720

721 **Conflict of interest** The authors declare that they have no conflict of interest.

722

723 **Human and animals rights** This article does not contain any studies with human participants or
724 animals performed by any of the authors.

725

726 **Author contributions** The manuscript was written through contributions of all authors. All
727 authors have given approval to the final version of the manuscript.

728

729 **Informed consent** Informed consent was obtained from all individual participants included in
730 the study.

731

732 **Supplementary Information**

733 The online version contains supplementary material available at <https://doi.org/>

734

735 **References**

736

737 Andresen M, Johansson LS, Tanem BS, Stenius P (2006) Properties and characterization of
738 hydrophobized microfibrillated cellulose. *Cellulose* 13:665–677. [https://doi.org/10.1007/s10570-](https://doi.org/10.1007/s10570-006-9072)
739 [006-9072](https://doi.org/10.1007/s10570-006-9072)

740 Auzel F (2004) Upconversion and anti-Stokes processes with f and d ions in solids. *Chem*
741 *Rev* 104(1):139–174. <https://doi.org/10.1021/cr020357g>

742 Beari F, Brand M, Jenkner P, Lehnert R, Metternich HJ, Monkiewicz J, Siesler HW (2001)
743 Organofunctional alkoxy silanes in dilute aqueous solution: new accounts on the dynamic
744 structural mutability. *J Organomet Chem* 625(2):208–216. [https://doi.org/10.1016/S0022-](https://doi.org/10.1016/S0022-328X(01)00650-7)
745 [328X\(01\)00650-7](https://doi.org/10.1016/S0022-328X(01)00650-7)

746 Belyaev AN, Chabushkin AN, Khrushchalina SA, Kuznetsova OA, Lyapin AA, Romanov
747 KN, Ryabochkina PA (2016) Investigation of endovenous laser ablation of varicose veins in
748 vitro using 1.885 μm laser radiation. *Lasers in Medical Science* 31:503–510.
749 <https://doi.org/10.1007/s10103-016-1877-z>

750 Brites CDS, Kuznetsov SV, Konyushkin VA, Nakladov AN, Fedorov PP, Carlos L D (2020)
751 Simultaneous measurement of the emission quantum yield and local temperature: the illustrative
752 example of $\text{SrF}_2:\text{Yb}^{3+}/\text{Er}^{3+}$ single crystals. *European Journal of Inorganic Chemistry* 17:1555–
753 1561. <https://doi.org/10.1002/ejic.202000113>

754 Chen YW, Lee HV, Juan JC, Phang SM (2016) Production of new cellulose nanomaterial
755 from red algae marine biomass *Gelidium elegans*. *Carbohydr Polym* 151:1210–1219.
756 <https://doi.org/10.1016/j.carbpol.2016.06.083>

757 Culler SR, Ishida H, Koenig JL (1985) Structure of silane coupling agents adsorbed on
758 silicon powder. *Journal of Colloid and Interface Science* 106(2):334–346.
759 [https://doi.org/10.1016/s0021-9797\(85\)80007-2](https://doi.org/10.1016/s0021-9797(85)80007-2)

760 Dai L, Wang Y, Zou X, Chen Z, Liu H, Ni Y (2020) Ultrasensitive Physical, Bio, and
761 Chemical Sensors Derived from 1-, 2-, and 3-D Nanocellulosic Materials. *Small*
762 16(13):1906567. <https://doi.org/10.1002/smll.201906567>

763 De France K, Zeng Z, Wu T, Nyström G (2020) Functional Materials from Nanocellulose:
764 Utilizing Structure-Property Relationships in Bottom-Up Fabrication. *Advanced Materials*.
765 <https://doi.org/10.1002/adma.202000657>

766 Delone NB (1993) *Basics of Interaction of Laser Radiation with Matter*. Editions Frontières,
767 France

768 Dias OAT, Konar S, Leão AL, Yang W, Tjong J, Sain M (2020) Current State of
769 Applications of Nanocellulose in Flexible Energy and Electronic Devices. *Frontiers in Chemistry*
770 8:420. <https://doi.org/10.1002/smll.201906567>

771 Dong H, Sun L-D, Yan C-H (2013) Basic understanding of the lanthanide related
772 upconversion emissions. *Nanoscale* 5:5703–5714. <https://doi.org/10.1039/C3NR34069D>

773 Eichhorn SJ (2018) Cellulose nanofibres for photonics and plasmonics. *Current Opinion in*
774 *Green and Sustainable Chemistry* 12:1-7. <https://doi.org/10.1016/j.cogsc.2018.03.010>

775 Emmert LA, Rudolph W (2014) Femtosecond Laser-Induced Damage in Dielectric
776 Materials. In: Ristau D (ed) *Laser-Induced Damage in Optical Materials*, Taylor & Francis
777 Group, pp 127–152. <https://doi.org/10.1201/b17722>

778 Fedorov PP, Luginina AA, Kuznetsov SV, Osiko VV (2011) Nanofluorides. *J Fluor Chem*
779 132:1012–1039. <https://doi.org/10.1016/j.jfluchem.2011.06.025>

780 Fedorov PP, Luginina AA, Rozhnova YA, Kuznetsov SV, Voronov VV, Uvarov OV,
781 Pynenkov AA, Nishchev KN (2017) Preparation of nanodispersed fluorite-type $\text{Sr}_{1-x}\text{R}_x\text{F}_{2+x}$ (R=
782 Er, Yb, Ho) phases from citrate solutions. *J Fluor Chem* 194:8–15.
783 <https://doi.org/10.1016/j.jfluchem.2016.12.003>.

784 Fedorov PP, Luginina AA, Kuznetsov SV, Voronov VV, Lyapin AA, Ermakov AS,
785 Pominova DV, Yaprntsev AD, Ivanov VK, Pynenkov AA, Nishchev KN (2019) Composite up-
786 conversion luminescent films containing a nanocellulose and $\text{SrF}_2:\text{Ho}$ particle. *Cellulose*
787 26:2403–2423. <https://doi.org/10.1007/s10570-018-2194-4>.

788 Fedorov PP, Luginina AA, Kuznetsov SV, Voronov VV, Yaprntsev AD, Lyapin AA,
789 Pynenkov AA, Nishchev KN, Chernova EV, Petukhov DI, Kuryakov VN, Gainutdinov RV,
790 Ivanov VK (2020) Hydrophobic up-conversion carboxylated nanocellulose/fluoride phosphor
791 composite films modified with alkyl ketene dimer. *Carbohydr Polym* 250:116866,
792 <https://doi.org/10.1016/j.carbpol.2020.116866>

793 Fischer S, Ivaturi A, Jakob P, Kramer KW, Martin-Rodriguez R, Mejerink A, et al (2018)
794 Upconversion solar cell measurements under real sunlight. *Optical Materials* 84:389–395.
795 <https://doi.org/10.1016/j.optmat.2018.05.072>.

796 Fukuzumi H, Saito T, Okita Y, Isogai A (2010) Thermal stabilization of TEMPO-oxidized
797 cellulose. *Polymer Degradation and Stability* 95(9):1502–1508.
798 <https://doi.org/10.1016/j.polymdegradstab.2010.06.015>

799 Guan Q, Song R, Wu W et al (2018) Fluorescent CdTe-QD-encoded nanocellulose
800 microspheres by green spraying method. *Cellulose* 25:7017–7029.
801 <https://doi.org/10.1007/s10570-018-2065-z>

802 Habibi Y, Chanzy H, Vignon MR (2006) TEMPO-mediated surface oxidation of cellulose
803 whiskers. *Cellulose* 13(6):679–687. <https://doi.org/10.1007/s10570-006-9075-y>

804 Hai J, Li T, Su J, Liu W, Ju Y, Wang B, Hou, Y (2018) Reversible Response of Luminescent
805 Terbium(III)-Nanocellulose Hydrogels to Anions for Latent Fingerprint Detection and
806 Encryption. *Angew Chem Int Ed* 57(23):6786–6790. <https://doi.org/10.1002/anie.201800119>

807 Hokkanen S, Repo E, Suopajarvi T et al (2014) Adsorption of Ni(II), Cu(II) and Cd(II) from
808 aqueous solutions by amino modified nanostructured microfibrillated cellulose. *Cellulose*
809 21:1471–1487. <https://doi.org/10.1007/s10570-014-0240-4>

810 Indarti E, Marwan, Rohaizu R, Wanrosli WD (2019) Silylation of TEMPO oxidized
811 nanocellulose from oil palm empty fruit bunch by 3-aminopropyltriethoxysilane. *Int J Biol*
812 *Macromol* 135:106–112. <https://doi.org/10.1016/j.ijbiomac.2019.05.161>

813 Ishida H, Chiang C, Koenig JL (1982) The structure of aminofunctional silane coupling
814 agents: 1. γ -Aminopropyltriethoxysilane and its analogues. *Polymer* 23(2):251–257.
815 [https://doi.org/10.1016/0032-3861\(82\)90310-x](https://doi.org/10.1016/0032-3861(82)90310-x)

816 Jiang F, Han S, Hsieh YL (2013) Controlled defibrillation of rice straw cellulose and
817 selfassembly of cellulose nanofibrils into highly crystalline fibrous materials. *RSC Advances*
818 3(30):12366–12375. <https://doi.org/10.1039/c3ra41646a>

819 Jiang H, Zhou D, Qu D, Chu G, Xu W, Song H, Xu Y (2016) Self-organized helical
820 superstructure of photonic cellulose loaded with upconversion nanoparticles showing modulated
821 luminescence. *RSC Advances* 6:76231–76236. <https://doi.org/10.1039/C6RA13894B>

822 Johansson LS, Tammelin T, Campbell JM, Setälä H, Österberg M (2011) Experimental
823 evidence on medium driven cellulose surface adaptation demonstrated using nanofibrillated
824 cellulose. *Soft Matter* 7:10917–10924. <https://doi.org/10.1039/C1SM06073B>

825 Khanjanadeh H, Behrooz R, Bahramifar N, Gindl-Altmutter W, Bacher M, Edler M,
826 Griesser T (2018) Surface Chemical Functionalization of Cellulose Nanocrystals by 3-
827 aminopropyltriethoxysilane. *Int J Biol Macromol* 106:1288–1296.
828 <http://dx.doi.org/10.1016/j.ijbiomac.2017.08.136>

829 Kim J, Holing GJ, Somorjai GA (2011) Curing Induced Structural Reorganization and
830 Enhanced Reactivity of Amino-Terminated Organic Thin Films on Solid Substrates:
831 Observations of Two Types of Chemically and Structurally Unique Amino Groups on the
832 Surface. *Langmuir* 27:5171–5175. <https://doi.org/10.1021/la2007205>

833 Kontturi E, Laaksonen P, Linder MB, Nonappa, Gröschel AH, Rojas OJ, Ikkala O (2018)
834 Advanced Materials through Assembly of Nanocelluloses. *Advanced Materials* 30(24):1703779.
835 <https://doi.org/10.1002/adma.201703779>.

836 Li XM, Reinhoudt D, Crego-Calama M (2007) What do we need for a superhydrophobic
837 surface? A review on the recent progress in the preparation of superhydrophobic surfaces.
838 *Chemical Society Reviews* 36(8):1350–1368. <https://doi.org/10.1039/B602486F>

839 Li X, Hu Y (2019) Luminescent films functionalized with cellulose nanofibrils/CdTe
840 quantum dots for anti-counterfeiting applications. *Carbohydr Polym* 203:167–175.
841 <https://doi.org/10.1016/j.carbpol.2018.09.028>

842 Li X, Zou L, Wu G, Shen J (2014) Laser-induced damage on ordered and amorphous sol-gel
843 silica coatings. *Optical Materials Express* 4(12):2478–2484.
844 <https://doi.org/10.1364/ome.4.002478>

845 Liang CY, Marchessault RH (1959) Infrared spectra of crystalline polysaccharides. II.
846 Native celluloses in the region from 640 to 1700 cm.⁻¹. *Journal of Polymer Science* 39(135):269–
847 278. <https://doi.org/10.1002/pol.1959.1203913521>

848 Liang L, Qin X, Zheng K, Liu X (2019) Energy Flux Manipulation in Upconversion
849 Nanosystems. *Accounts of Chemical Research* 52(1):228-236.
850 <https://doi.org/10.1021/acs.accounts.8b00469>

851 Lichtenstein K, Lavoine N (2017) Toward a deeper understanding of the thermal degradation
852 mechanism of nanocellulose. *Polym Degrad Stab* 146:53–60.
853 <https://doi.org/10.1016/j.polymdegradstab.2017.09.018>

854 Lizundia E, Puglia D, Nguyen T-D, Armentano I (2020) Cellulose nanocrystal based
855 multifunctional nanohybrids. *Progress in Materials Science* 112:100668.
856 <https://doi.org/10.1016/j.pmatsci.2020.100668>

857 Lyapin AA, Kuznetsov SV, Ryabochkina PA, Merculov AP, Chernov MV, Ermakova YA,
858 Luginina AA, Fedorov PP (2017) Upconversion luminescence of $\text{Ca}_{1-x}\text{Ho}_x\text{F}_{2+x}$ and
859 $\text{Sr}_{0.98-x}\text{Er}_{0.02}\text{Ho}_x\text{F}_{2.02+x}$ powders upon excitation by an infrared laser. *Laser Physics Letters*
860 14:076003 (5pp). <https://doi.org/10.1088/1612-202X/aa7418>.

861 Masmoudi M, Rahal C, Abdelmouleh M, Abdelhedi R (2013) Hydrolysis process of γ -APS
862 and characterization of silane film formed on copper in different conditions. *Appl Surf Sci*
863 286:71–77. <https://doi.org/10.1016/j.apsusc.2013.09.018>

864 Nguyen TD, Hamad WY, MacLachlan MJ (2017) Near-IR-Sensitive Upconverting
865 Nanostructured Photonic Cellulose Films. *Adv Opt Mater* 5:1600514 (7 pp).
866 <https://doi.org/10.1002/adom.201600514>.

867 Oh SY, Yoo DI, Shin Y, Kim HC, Kim HY, Chung YS, Park WH, Youk JH (2005)
868 Crystalline structure analysis of cellulose treated with sodium hydroxide and carbon dioxide by
869 means of X-ray diffraction and FTIR spectroscopy. *Carbohydrate Research* 340(15):2376-2391.
870 <http://dx.doi.org/10.1016/j.carres.2005.08.007>

871 Okita Y, Saito T, Isogai A (2010) Entire surface oxidation of various cellulose microfibrils
872 by TEMPO-mediated oxidation. *Biomacromolecules* 11(6):1696–1700.
873 <https://doi.org/10.1021/bm100214b>

874 Orsolini P, Antonini C, Stojanovic A, Malfait WJ, Caseri WR, Zimmermann T (2018)
875 Superhydrophobicity of nanofibrillated cellulose materials through polysiloxane nanofilaments.
876 *Cellulose* 25:1127–1146. <https://doi.org/10.1007/s10570-017-1636-8>

877 Ovsyankin VV, Feofilov PP (1966) Mechanism of Summation of Electronic Excitations in
878 Activated Crystals. *JETP Lett* 3:322–323.

879 Pavia DL, Lampman GM, Kriz GS, Vyvyan JR (2009) *Introduction to Spectroscopy*. 4th
880 edn. Belmont, USA

881 Peña-Alonso R, Rubio F, Rubio J (2005) The Role of γ -Aminopropyltriethoxysilane (γ -
882 APS) on Thermal Stability of TEOS-PDMS Ormosils. *J Sol-Gel Sci Technol* 36:77–85.
883 <https://doi.org/10.1007/s10971-005-3408-4>

884 Pereira ALS, Feitosa JPA, Morais JPS, Rosa MF (2020) Bacterial cellulose aerogels:
885 Influence of oxidation and silanization on mechanical and absorption properties. *Carbohydr*
886 *Polym* 250:116927. <https://doi.org/10.1016/j.carbpol.2020.116927>

887 Peresin MS, Kammiovirta K, Heikkinen H, Johansson LS, Vartiainen J, Setälä H, Österberg
888 M, Tammelin T (2017) Understanding the mechanisms of oxygen diffusion through surface
889 functionalized nanocellulose films. *Carbohydr Polym* 174:309–317.
890 <https://doi.org/10.1016/j.carbpol.2017.06.066>

891 Qiao B, Wang T-J, Gao H, Jin Y (2015) High density silanization of nano-silica particles
892 using γ -aminopropyltriethoxysilane (APTES). *Applied Surface Science* 351:646–654.
893 <https://doi.org/10.1016/j.apsusc.2015.05.174>

894 Qin X, Liu X, Huang W, Bettinelli M, Liu X (2017) Lanthanide activated phosphors based
895 on 4f–5d optical transitions: theoretical and experimental aspects. *Chem Rev* 117:4488–4527.
896 <https://doi.org/10.1021/acs.chemrev.6b00691>

897 Rachini A, Le Troedec M, Peyratout C, Smith A (2012) Chemical modification of hemp
898 fibers by silane coupling agents. *J Appl Polym Sci* 123(1):601–610.
899 <https://doi.org/10.1002/app.34530>

900 Reig DS, Grauel B, Konyushkin VA, Nakladov AN, Fedorov PP, Busko D, Howard IA,
901 Richards BS, Resch-Genger U, Kuznetsov SV, Turshatov A, Würth C (2020) Upconversion
902 properties of SrF₂:Yb³⁺,Er³⁺ single crystals. *J Mater Chem C* 8:4093-4101.
903 <https://doi.org/10.1039/C9TC06591A>

904 Robles E, Csóka L, Labidi J. (2018) Effect of Reaction Conditions on the Surface
905 Modification of Cellulose Nanofibrils with Aminopropyl Triethoxysilane. *Coatings* 8(4):139.
906 <https://doi.org/10.3390/coatings8040139>

907 Rol F, Belgacem MN, Gandini A, Bras J (2019) Recent advances in surface-modified
908 cellulose nanofibrils. *Progress in Polymer Science* 88:241-264.
909 <https://doi.org/10.1016/j.progpolymsci.2018.09.002>

910 Sai H, Fu R, Xing L, Xiang J, Li Z, Li F, Zhang T (2015) Surface modification of bacterial
911 cellulose aerogels' web-like skeleton for oil/water separation. *ACS Appl Mater Interfaces*
912 7(13):7373-7381. <https://doi.org/10.1021/acsami.5b00846>

913 Salon M-CB, Gerbaud G, Abdelmouleh M, Bruzzese C, Boufi S, Belgacem MN (2007)
914 Studies of interactions between silane coupling agents and cellulose fibers with liquid and solid-
915 state NMR. *Magnetic Resonance in Chemistry* 45(6):473-483. <https://doi.org/10.1002/mrc.1994>

916 Salon M-CB, Belgacem MN (2010) Competition between hydrolysis and condensation
917 reactions of trialkoxysilanes, as a function of the amount of water and the nature of the organic
918 group. *Colloids Surf A Physicochem Eng Asp* 366:147-154.
919 <https://doi.org/10.1016/j.colsurfa.2010.06.002>

920 Scholle K, Lamrini S, Koopmann P, Fuhrberg P (2010) 2 μm laser sources and their possible
921 applications. In: Pal B (ed) *Frontiers in Guided Wave Optics and Optoelectronics*, InTech,
922 London, pp 471-500. <https://doi.org/10.5772/39538>

923 Tan Y, Liu Y, Chen W, Liu Y, Wang Q, Li J, Yu H (2016) Homogeneous Dispersion of
924 Cellulose Nanofibers in Waterborne Acrylic Coatings with Improved Properties and Unreduced
925 Transparency. *ACS Sustainable Chem Eng* 4(7):3766-3772.
926 <https://doi.org/10.1021/acssuschemeng.6b00415>

927 Thomas B, Raj MC, Athira KB, Rubiyah MH, Joy J, Moores A, Drisko GL, Sanchez C
928 (2018) Nanocellulose, a Versatile Green Platform: From Biosources to Materials and Their
929 Applications. *Chem Rev* 118(24):11575-11625 <https://doi.org/10.1021/acs.chemrev.7b00627>

930 Vandenberg ET, Bertilsson L, Liedberg B, Uvdal K, Erlandsson R, Elwing H, Lundström I
931 (1991) Structure of 3-aminopropyl triethoxy silane on silicon oxide. *Journal of Colloid and*
932 *Interface Science* 147(1):103-118. [https://doi.org/10.1016/0021-9797\(91\)90139-y](https://doi.org/10.1016/0021-9797(91)90139-y)

933 Verber CM, Grieser DR, Jones WH (1971) Cooperative and sequential excitation of red
934 fluorescence of Ho³⁺ in CaF₃. *Journal of Applied Physics* 42(7):2767-2769.
935 <https://doi.org/10.1063/1.1660621>.

936 Vicente AT, Araújo A, Mendes MJ, Nunes D, Oliveira MJ, Sanchez-Sobrado O, Ferreira
937 MP, Águas H, Fortunato E, Martins R (2018) Multifunctional cellulose-paper for light harvesting
938 and smart sensing applications. *J Mater Chem C* 6:3143-3181.
939 <https://doi.org/10.1039/C7TC05271E>

940 Voronova MI, Surov OV, Kraev AS, Isaeva DA, Mityukhina IS, Zakharov AG (2017)
941 Template synthesis of mesoporous silicas with the use of nanocrystalline cellulose. *Colloid J*
942 79:18-25. <https://doi.org/10.1134/S1061933X17010148>

943 Wang H, Pei Y, Qian X, An X (2020) Eu-metal organic framework@TEMPO-oxidized
944 cellulose nanofibrils photoluminescence film for detecting copper ions. *Carbohydr Polym*
945 236:116030. <https://doi.org/10.1016/j.carbpol.2020.116030>

946 Wenzel RN (1936) Resistance of Solid Surfaces to Wetting by Water. *Ind Eng Chem*
947 28(8):988-994. <https://doi.org/10.1021/ie50320a024>

948 Wood R (2014) Laser-Induced Damage by Thermal Effects. *Laser-Induced Damage in*
949 *Optical Materials*. In: Ristau D (ed) *Laser-Induced Damage in Optical Materials*, CRC Press,
950 Taylor & Francis Group, pp 9-24. <https://doi.org/10.1201/b17722-4>

951 Xiong R, Yu S, Smith MJ, Zhou J, Kreckler M, Zhang L, Nepal D, Bunning TJ, Tsukruk VV
952 (2019) Self-Assembly of Emissive Nanocellulose/Quantum Dots Nanostructures for Chiral
953 Fluorescent Materials. *ACS Nano* 13(8):9074–9081. <https://doi.org/10.1021/acsnano.9b03305>
954 Xue B, Zhang Z, Sun Y, Wang J, Jiang H, Du M, Chi C, Li X. (2018) Near-infrared
955 emissive lanthanide hybridized nanofibrillated cellulose nanopaper as ultraviolet filter. *Carbohydr*
956 *Polym* 186:176–183. <https://doi.org/10.1016/j.carbpol.2017.12.088>
957 Yang Q, Zhang C, Shi Z, Wang J, Xiong C, Saito T, Isogai A (2018) Luminescent and
958 Transparent Nanocellulose Films Containing Europium Carboxylate Groups as Flexible
959 Dielectric Materials. *ACS Appl Nano Mater* 1(9):4972–4979.
960 <https://doi.org/10.1021/acsanm.8b01112>
961 Zhang S, Liu G, Chang H, Li X, Zhang Z (2019) Optical haze nanopaper enhanced
962 ultraviolet harvesting for direct soft-fluorescent emission based on lanthanide complex assembly
963 and oxidized cellulose nanofibrils. *ACS Sustain Chem Eng* 7(11):9966–9975.
964 <https://doi.org/10.1021/acssuschemeng.9b00970>
965 Zhang Z, Chang H, Xue B, Han Q, Lü X, Zhang S, Li X, Zhu X, Wong W, Li K (2017) New
966 transparent flexible nanopaper as ultraviolet filter based on red emissive Eu(III) nanofibrillated
967 cellulose. *Opt Mater* 73:747–753. <https://doi.org/10.1016/j.optmat.2017.09.039>
968 Zhang Z, Chang H, Xue B, Zhang S, Li X, Wong WK, Li K, Zhu X (2018) Near-infrared
969 and visible dual emissive transparent nanopaper based on Yb(III)–carbon quantum dots grafted
970 oxidized nanofibrillated cellulose for anticounterfeiting applications. *Cellulose* 25:377–389.
971 <https://doi.org/10.1007/s10570-017-1594-1>
972 Zhao J, Wei Z, Feng X, Miao M, Sun L, Cao S, Shi L, Fang J (2014) Luminescent and
973 transparent nanopaper based on rare-earth up-converting nanoparticles grafted nanofibrillated
974 cellulose derived from garlic skin. *ACS Appl Mater Interfaces* 6:14945–14951.
975 <https://doi.org/10.1021/am5026352>
976 Zhou J, Liu Q, Feng W, Sun Y, Li F (2015) Upconversion Luminescent Materials: Advances
977 and Applications. *Chem Rev* 115(1):395–465. <https://doi.org/10.1021/cr400478f>

Figures

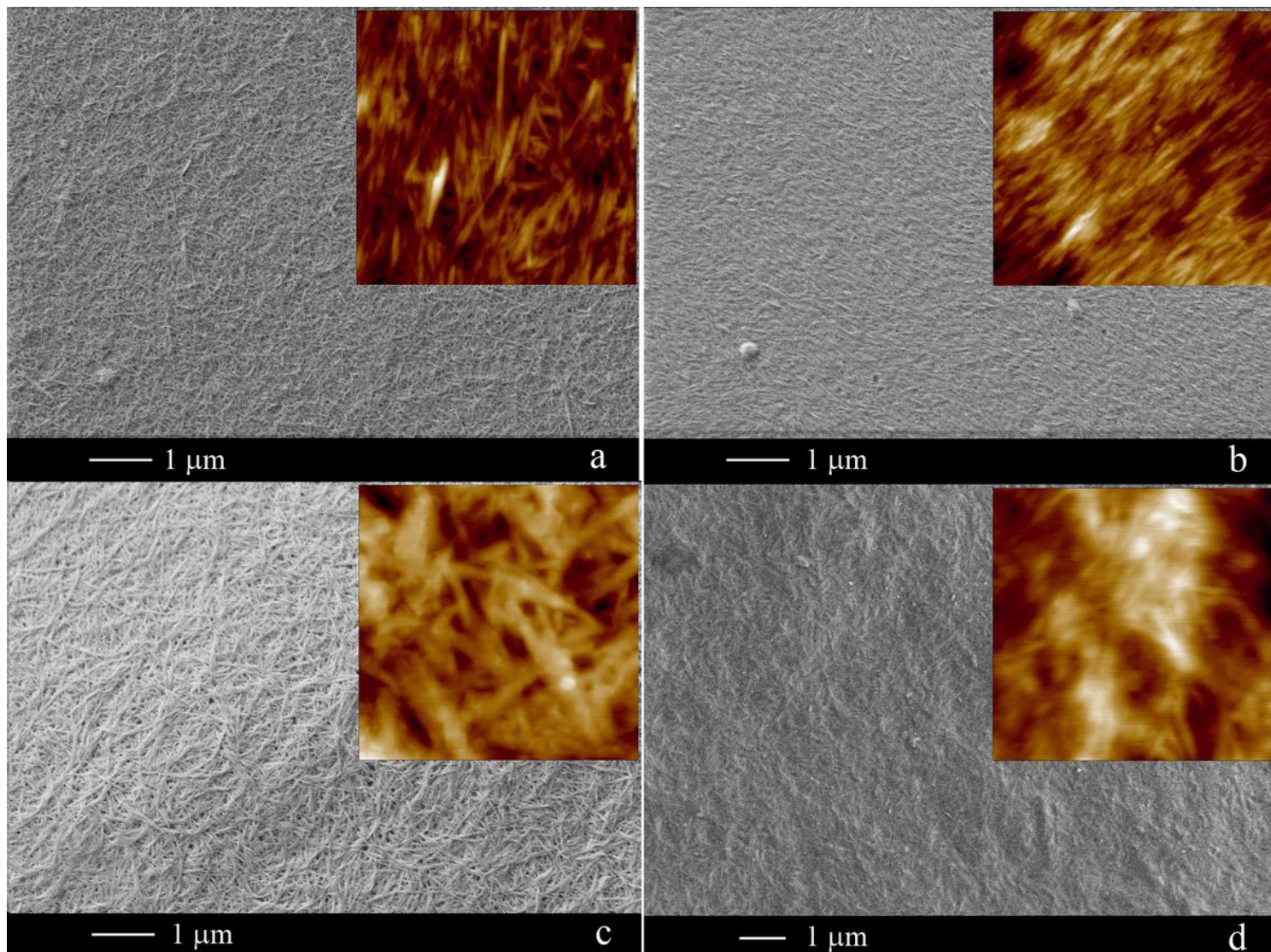


Figure 1

SEM images of 0.01 wt.% dispersions air-dried on a single-crystal silicon substrate: TOCNF (a), CNC (b). SEM images of films after thermal treatment at 105 °C: TOCNF-APS7.00 (c), TOCNF-bAPS7.0 (d). Insets show the corresponding film images obtained by AFM (1 μm × 1 μm scanning area)

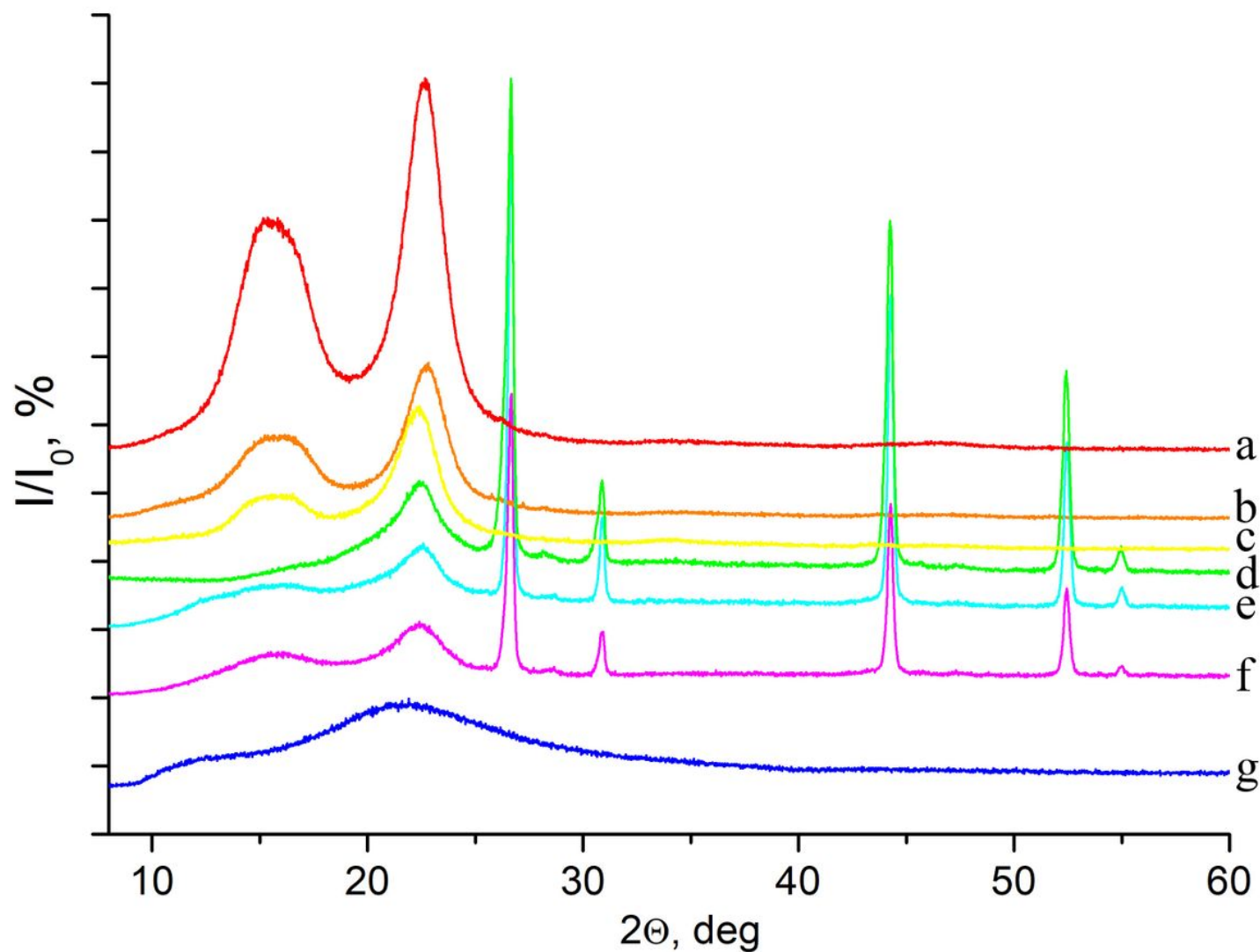


Figure 2

XRD patterns of the films after the thermal treatment at 105°C: TOCNF (a), TOCNF-bAPS7.0 (b); TOCNF-APS7.0 (c), TOCNF:3.5Ho (d), TOCNF:3.5Ho-bAPS7.0 (e), TOCNF:3.5Ho-APS7.0 (f), and of APS after thermal treatment at 700°C (g)

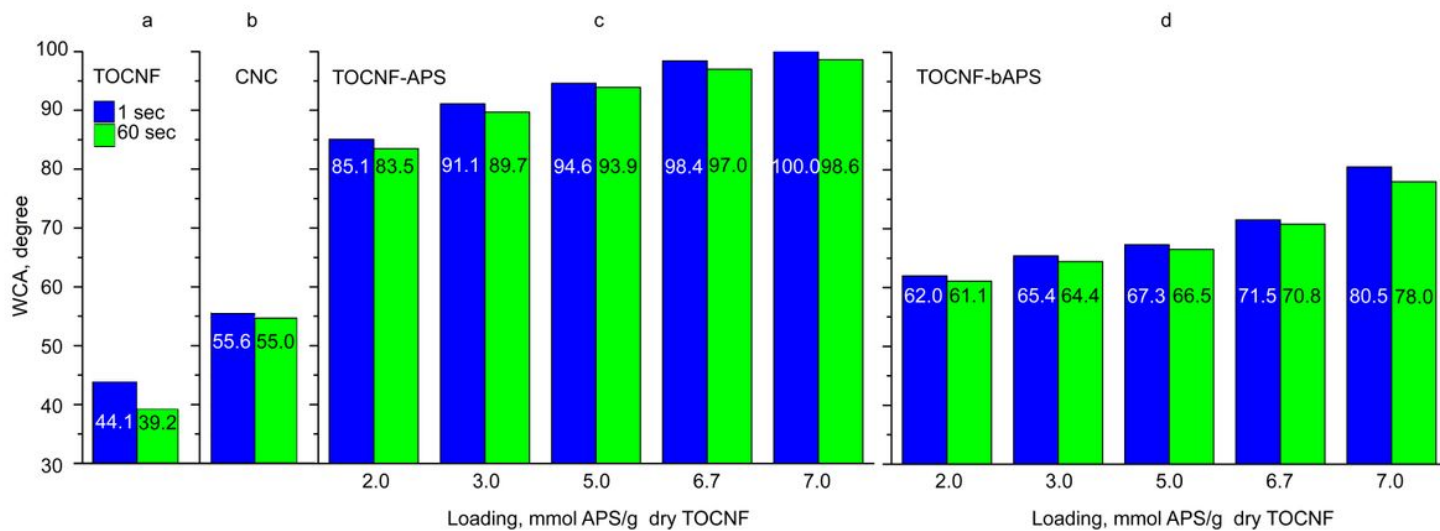


Figure 3

Correlation between the WCA for different nanocellulose films and the water droplet contact time

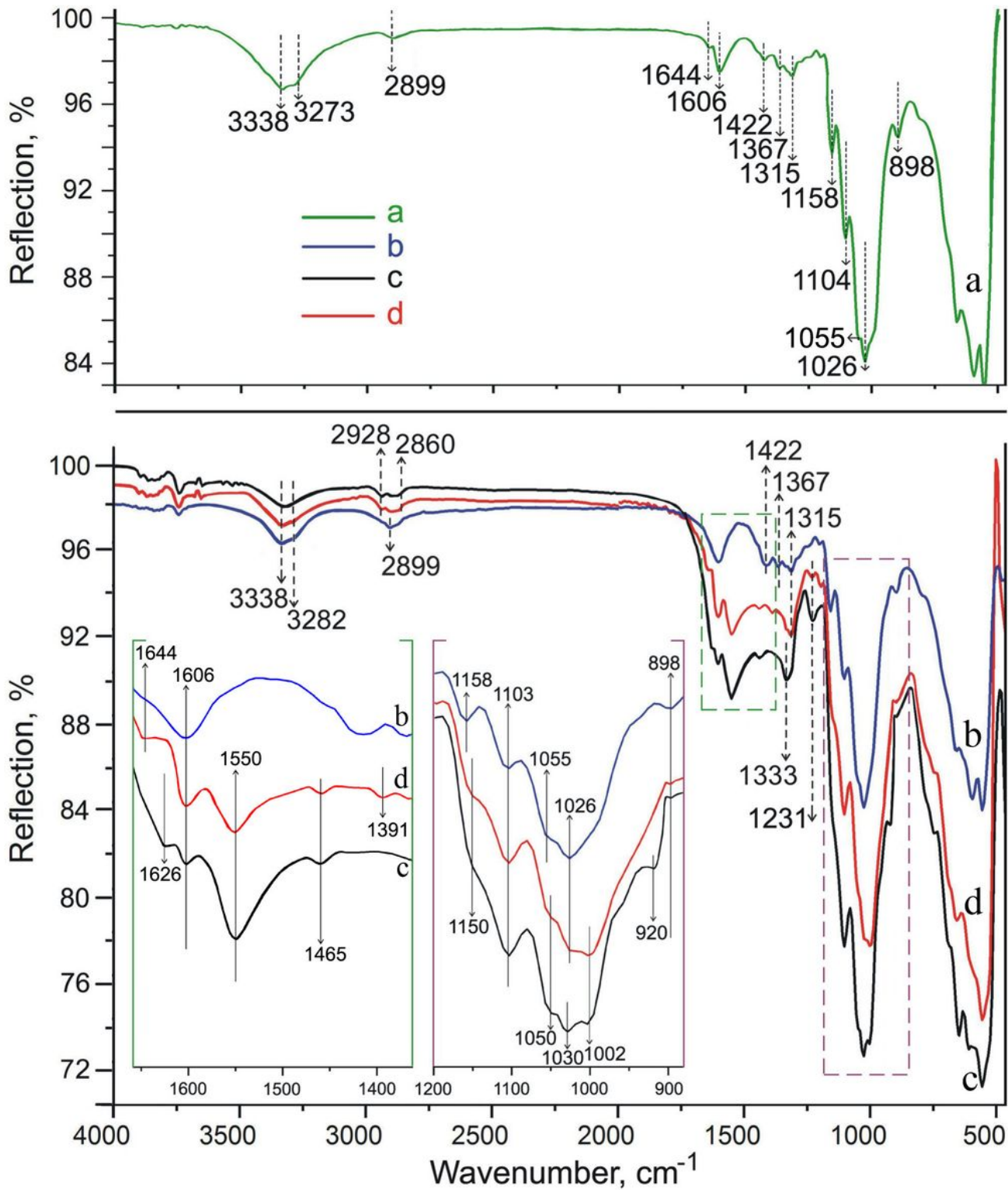


Figure 4

FTIR-spectra of TOCNF (a), TOCNF:3.5Ho (b), TOCNF:3.5Ho-APS7.0 (c), and TOCNF:3.5Ho-bAPS7.0 (d) films after their thermal treatment at 105°C

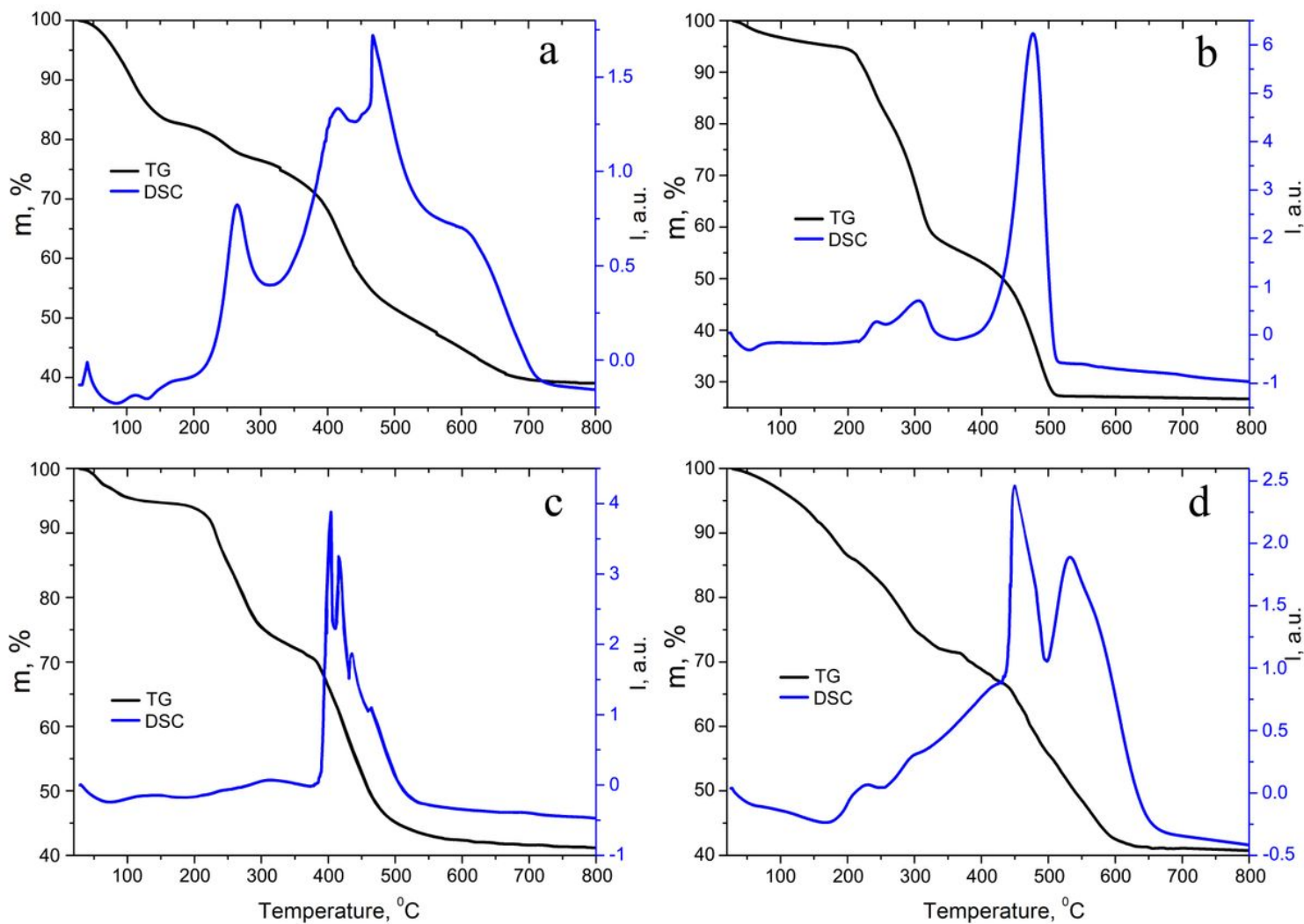


Figure 6

TG and DSC curves for APS (a) and TOCNF:3.3Ho (b), TOCNF:3.3Ho-APS6.7 (c), TOCNF:3.3Ho-bAPS6.7 (d) composite films after drying at 105°C



Figure 7

Appearance of the films: TOCNF (a), TOCNF-APS3.0 (b), TOCNF-APS7.0 (c) TOCNF:3.3Ho (d), TOCNF:3.5Ho (e), TOCNF:5.5 Ho (f), TOCNF:3.3Ho-APS3.0 (g), TOCNF:3.5Ho-APS7.0 (h), TOCNF:5.5Ho-APS6.0 (i)

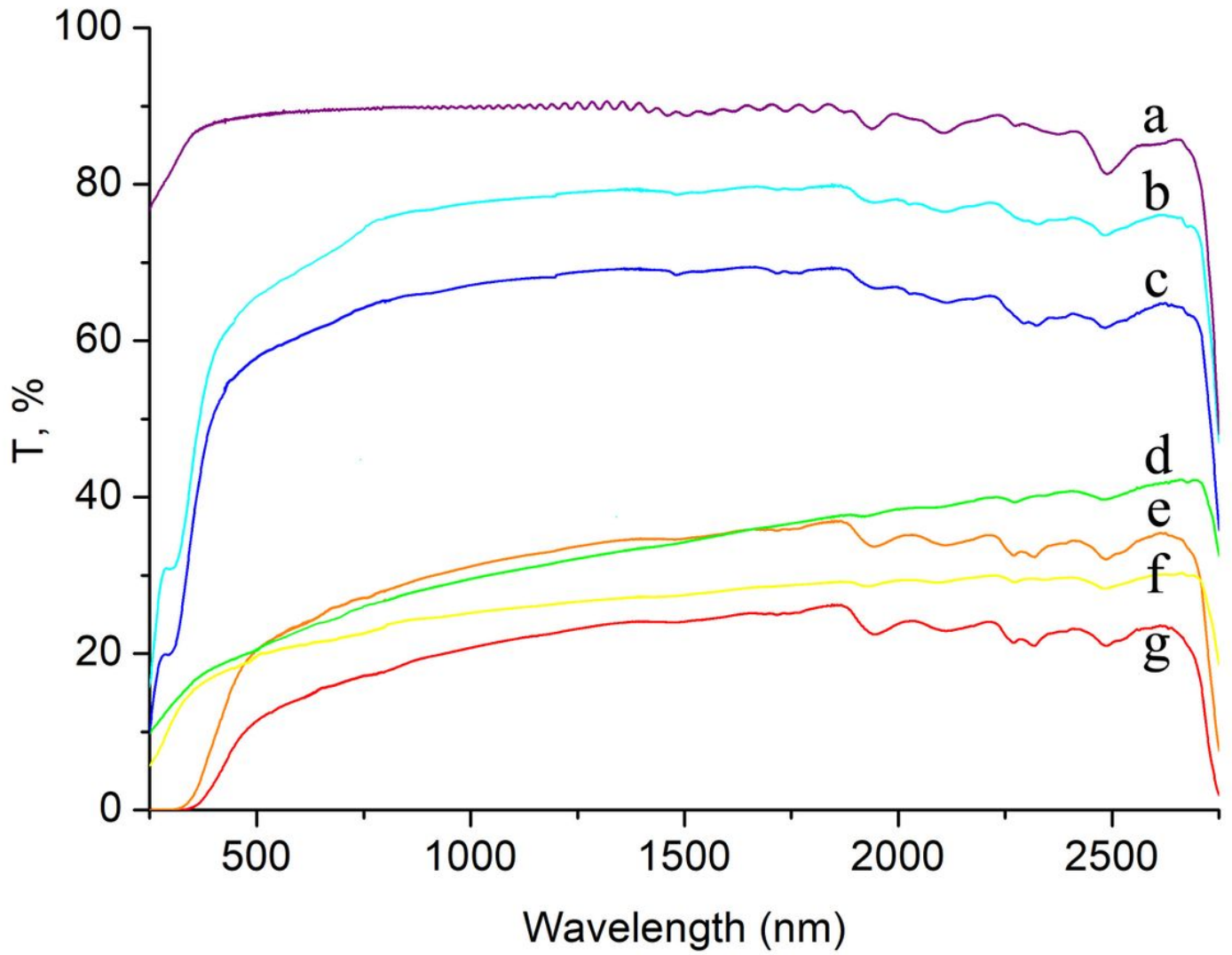


Figure 8

Transmission spectra of the films: TOCNF (a), TOCNF-APS3.0 (b), TOCNF-APS7.0 (c) TOCNF:3.3Ho (d), TOCNF:3.3Ho-APS3.0 (e), TOCNF:3.5Ho (f), TOCNF:3.5Ho-APS7.0 (g)

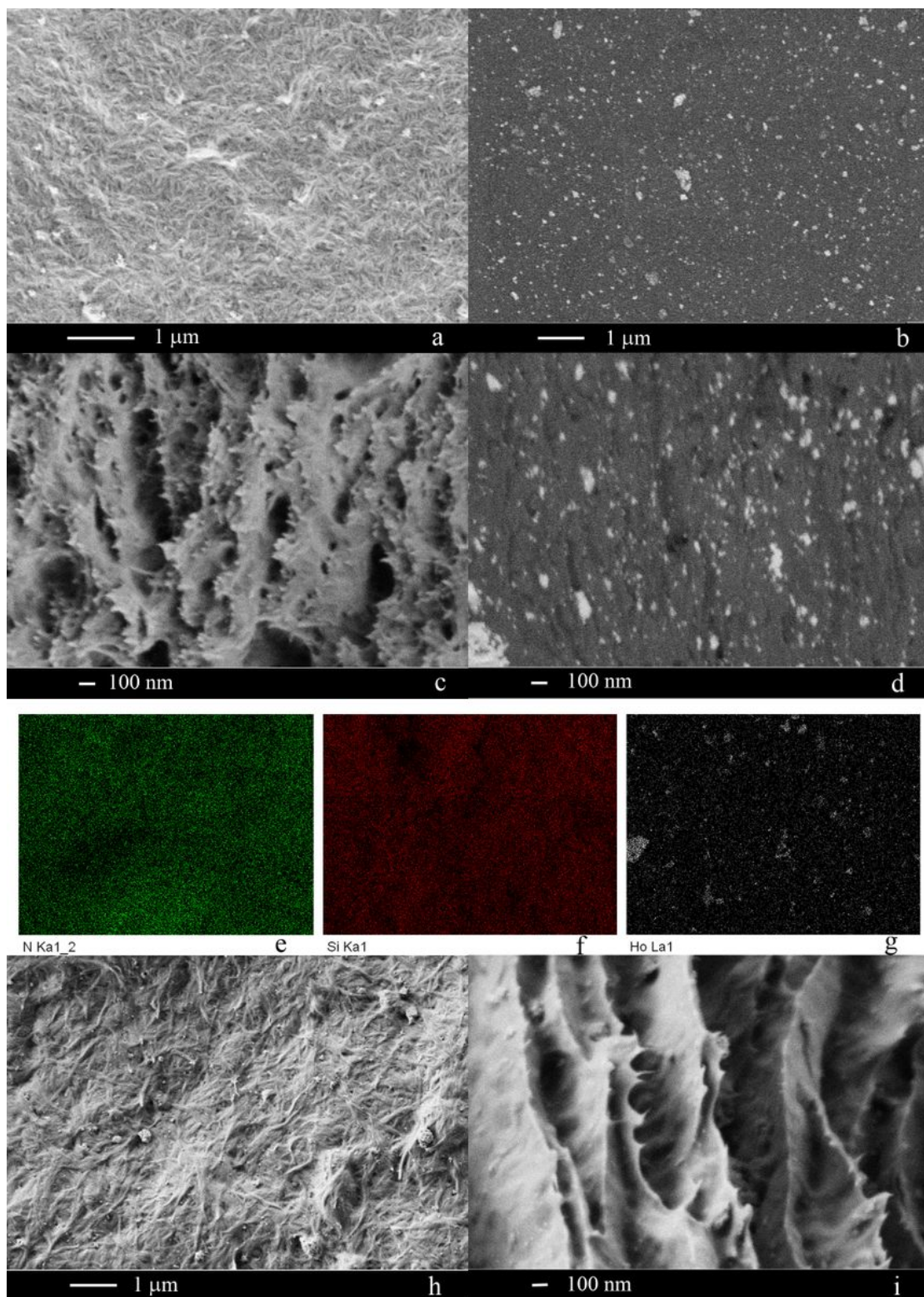


Figure 9

SEM images and EDX maps of TOCNF:3.3Ho-APS5.0 film: surface (a, b); cross-section (c, d); images in topographic contrast mode (a, c); images in Z-contrast mode (b, d); EDX maps for N (e), Si (f) and Ho (g) elements distribution across the surface. SEM images of TOCNF:3.3Ho-bAPS5.0 film surface (h) and cross-section (i)

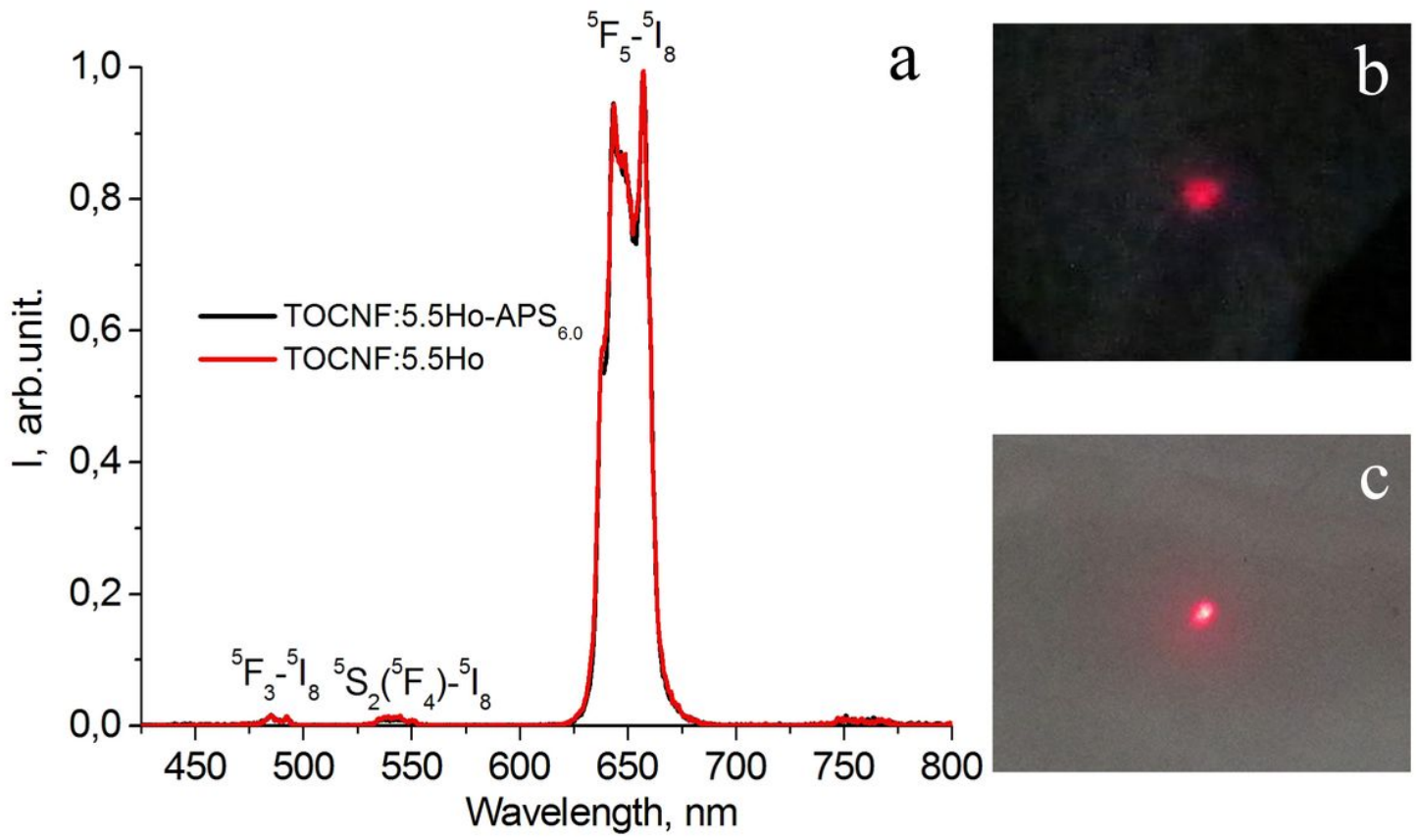


Figure 10

Up-conversion luminescence spectra of the composite films (a); and IR light visualization by the composite films: TOCNF:5.5Ho (b), TOCNF:5.5Ho-APS6.0 (c). Laser excitation of Ho³⁺ ions 5I₇ energy level at a wavelength of 1912 nm, beam diameter 10 μm

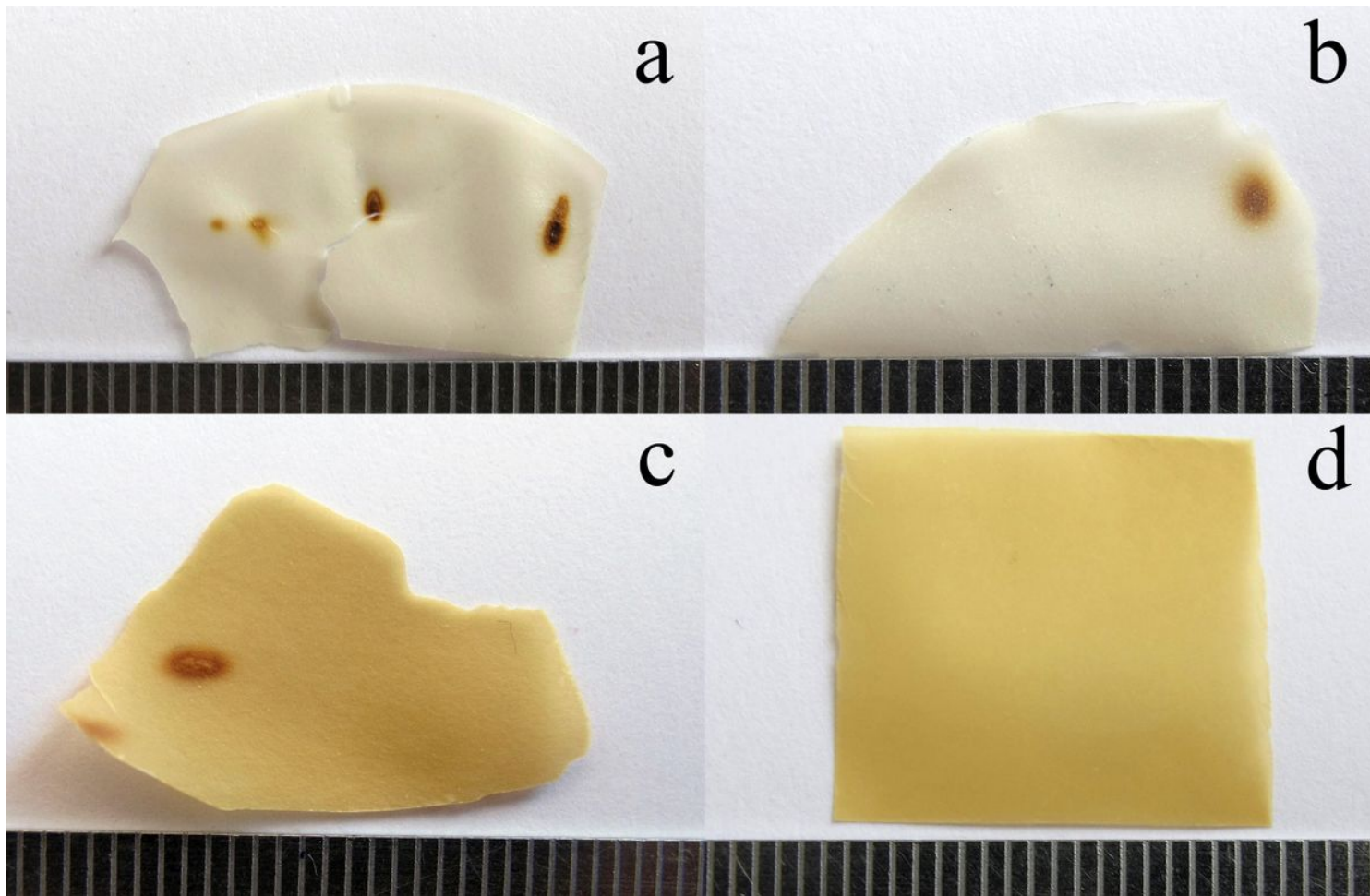


Figure 11

Images of composite films after laser irradiation with a power of 0.84 W: CNC:5.5Ho (a); TOCNF:5.5Ho (b); TOCNF:5.5Ho-bAPS6.0 (c); TOCNF:5.5Ho-APS6.0 (d)

Supplementary Files

This is a list of supplementary files associated with this preprint. Click to download.

- [graphabstract.jpg](#)
- [SupplementaryInformation.pdf](#)